Plasma beta effects on the edge magnetic field structure and divertor heat loads in Wendelstein 7-X high-performance scenarios

A. Knieps[1,*], Y. Suzuki[2,3], J. Geiger[4], A. Dinklage[4], S. Zhou[1,5], K. Rahbarnia[4], J. Schilling[4], U. Neuner[4], H. Thomsen[4], M. Jakubowski[4], R. Koenig[4], M. Endler[4], Y. Gao[4], A. Puig Sitjes[4], H. Niemann[4], M. Beurskens[4], S. Bozhenkov[4], the W7-X team , and Y. Liang[1,5]

[1]Forschungszentrum Jülich GmbH, Institut für Energie- und Klimaforschung Plasmaphysik, Partner of the Trilateral Euregio Cluster (TEC), Jülich, 52425, Germany
[2]National Institute for Fusion Science, National Institutes of Natural Sciences, 509-5292 Toki, Japan
[3]The Graduate University for Advanced Studies, SOKENDAI, 509-5292 Toki, Japan
[4]Max-Planck-Institut für Plasmaphysik, Greifswald, 17491, Germany
[5]International Joint Research Laboratory of Magnetic Confinement Fusion and Plasma Physics, State Key Laboratory of Advanced Electromagnetic Engineering and Technology, School of Electrical and Electronic Engineering, Huazhong University of Science and Technology, Wuhan, 430074, People's Republic of China
[*]Corresponding author a.knieps@fz-juelich.de

February 15, 2022

Abstract

To support the scenario design for the upcoming long-pulse high-performance campaign of Wendelstein 7-X, this work presents a study of high-beta full-field 3D equilibria obtained with the HINT code. For three magnetic configurations of different edge-ι, the effects of both overall pressure and pressure profile changes on the magnetic topology are analyzed. Anisotropic diffusion modeling is used to obtain estimates of the conductive heat load distribution both on the divertor and other plasma-facing components in finite-beta magnetic configurations. For the magnetic standard configuration, limitations of the model are outlined by comparing measured and predicted heatloads by performing a linear regression of the main strike-line position against various plasma parameters in both the experimental and the simulated device.

1 Introduction

In order to provide a stable baseline power source, future nuclear fusion reactor designs need to operate in a long-pulse high-performance regime. The Wendelstein 7-X experiment aims to demonstrate the viability of the HELIAS-type numerically optimized modular stellarator design as a candidate for high-performance long-pulse operation, being optimized for good confinement of medium- and high-energy particles in steady-state operation ([1]). In its upcoming experimental campaign, W7-X aims to demonstrate its long-pulse operation with up to 30 minute discharges and a volume-averaged plasma beta of 2-3%. Previous investigations into the MHD equi-libria of its configuration space indicate that the island divertor topology of its edge magnetic field can be adversely modified in medium- and high-beta operation [2]. Possible effects can range from small stochastization effects at the edge island separatrix to substantial changes in edge island size, poloidal phase and shape. Since heat- and particle-fluxes onto the plasma-facing components (PFCs) are mainly directed by the magnetic field, changes in the magnetic topology can have profound effects on the heat load distribution on the divertor (including the middle section with reduced heat load limits) and other PFCs. Most importantly, a change in topology can cause the direction of stationary heat loads onto non-divertor PFCs. Additionally, a significant reduction in the connection length could potentially degrade both the wetted area on the divertor and the shielding of the confined plasma core from (partially) ionized impurities, and potentially might make it more difficult to achieve the highly desirable detached divertor operation regime, which has already been reached in [3, 4, 5].

The MHD equilibrium and the edge topology have already been extensively studied in prior research works ([6, 7, 8, 9, 10, 11]) using various equilibrium codes, and potential implications of changes in the divertor topology were already extrapolated there. These studies mainly limit themselves to the geometry and topology of the magnetic field, but do not investigate the interaction of the finite-beta magnetic topologies with the geometry of the wall and divertor. This study expands upon the previous works by coupling the HINT code ([12, 13]) to an anisotropic diffusion model to obtain predictions for heat deposition profiles on the plasma-facing components

through convective scrape-off layer heat transport simulations, similar to the work performed in [14] and recently in [15] for VMEC-EXTENDER (which used a convective field line diffusion approach).

This paper presents a systematic study of plasma beta related changes in the edge magnetic topology at different values of the edge rotational transform (edge ι) and also investigates the impact of these changes on the heat flux distribution onto PFCs. After introducing the layout of W7-X and its island divertor (section 2) and the methodology employed to derive and analyze the finite-beta magnetic fields and divertor heat load simulations (section 3), it will showcase and discuss the simulated changes in the edge magnetic field and the divertor heat loads in section 4. Afterwards, the equilibrium simulations will be compared in section 5 with experimental observations for the most important part of the edge ι scan - the magnetic standard configuration before conclusion of the paper in section 6.

2 The island divertor of Wendelstein 7-X

W7-X is a fivefold stellarator-symmetric multi-configuration experiment. Its configuration space can mainly be varied by modifying the overall rotational transform, the magnetic mirror strength, and the average radial magnetic axis location [16]. This study focuses on the influence of the edge rotation transform, studying the low-iota-, standard, and high-iota configurations.

To control the heat and particle fluxes onto plasma-facing components, Wendelstein 7-X relies on a chain of magnetic islands (as shown in figure 1) positioned between the confined plasma core and the divertor target plates [17, 5]. Since the magnetic shear (radial gradient of the rotational transform) is low, these islands are wide and have a low internal rotational transform. Therefore the connection lengths in the scrape-off layer are sufficiently long (between $100\,\mathrm{m}$ and $500\,\mathrm{m}$) for perpendicular diffusion effects to play a role in widening the strike line and reducing the peak heat loads on the targets to a tolerable level. The geometry of this island chain is dependent on the edge ι value, with the high- (edge $\iota = {}^5\!/_4$) and low- (edge $\iota = {}^5\!/_6$) ι-configurations having four respectively six islands connected by a single magnetic flux tube, and the standard configuration (edge $\iota = {}^5\!/_5$) featuring five individual edge islands with their own magnetic flux tube each.

Mimicking the five-fold stellarator symmetry, the divertor consists of five mostly identical modules made out of two half-modules each [18]. The geometry of such a half-module is shown in figure 2, along with an example magnetic topology and related heat load simulation for the W7-X standard configuration. The main target (shown in grey and overlaid with a heat flux

distribution) consists of two target plates, a toroidally elongated horizontal target and a shorter vertical target plate. The strike line location on the horizontal target depends mainly on the rotation transform, with the tail (right half of figure 3) only being loaded in high-iota ($\iota = {}^n\!/_m = {}^5\!/_4$)-configuration, and heat loads otherwise being present on the front section (left part of figure 3) of the divertor target. A pumping gap for neutral particles is present between the vertical and horizontal target. The pumping volume of the divertor lies on the backside of the target plates, and is closed off by the divertor baffles, which are shown in figure 2 in transparent orange. While cooled, these baffles are not intended to bear a major share of the divertor heat flux and are (for the purpose of this study) limited to heat fluxes up to $0.25\,\mathrm{MW\,m^{-2}}$. Of additional relevance in this paper is the set of observation ports on the outboard side of the triangular plane, referred to as "U-port". As shown in figure 3, the divertor target is not a monolithic assembly but consists of 4 distinct sections. The vertical target, as well as the low- and high-iota horizontal targets are all rated for large heat-fluxes up to $10\,\mathrm{MW\,m^{-2}}$ [18]. The middle section separating the low- and high-iota targets however is only designed for a reduced heat load up to $0.5\,\mathrm{MW\,m^{-2}}$. During the first divertor campaign, the W7-X divertor was operated without active cooling. In the upcoming experimental campaign, the W7-X will for the first time operate in steady-state condition with a water-cooled divertor.
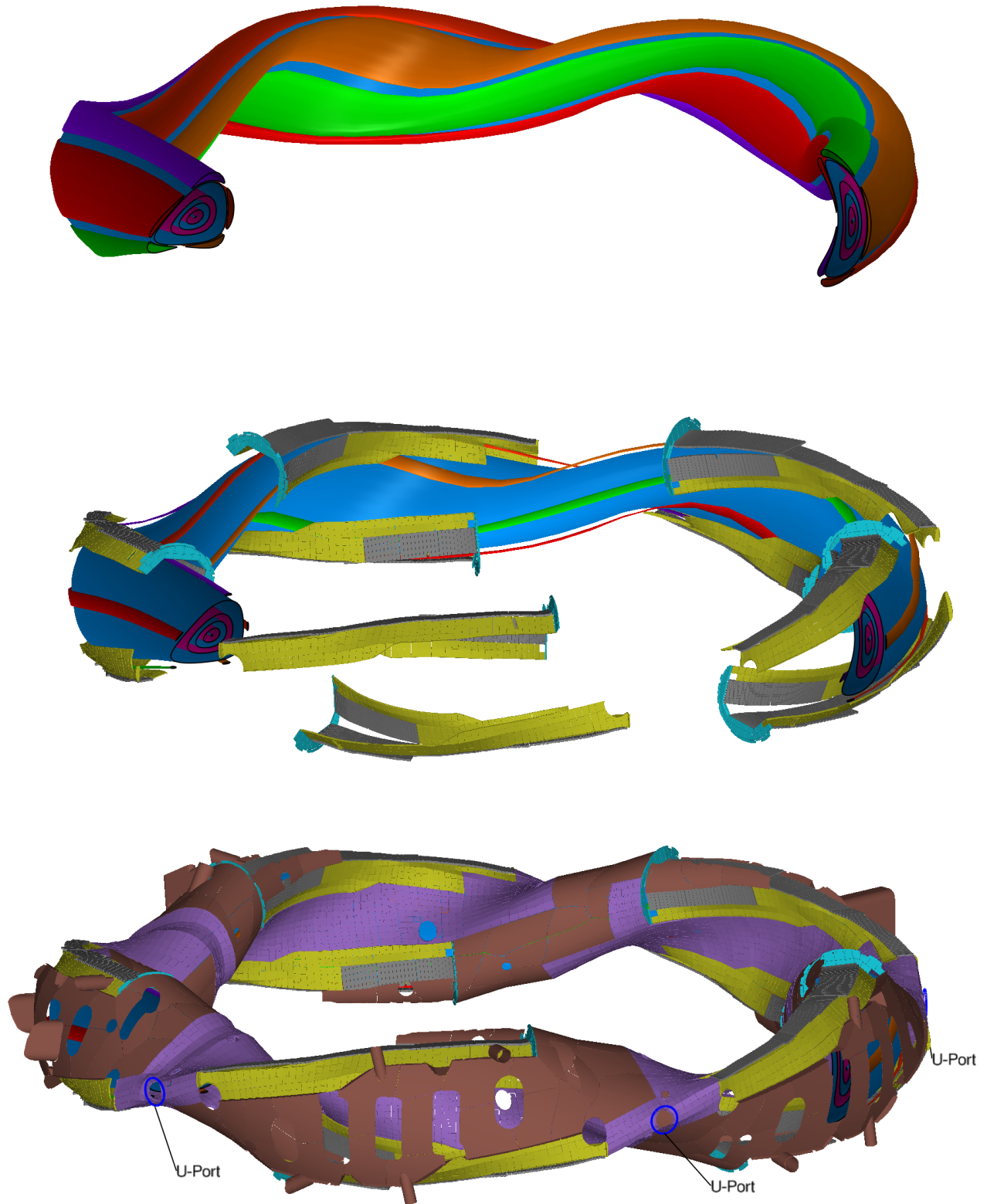
Figure 1: Overview of the magnetic flux surface structure of W7-X, including the islands and in blue the last closed flux surface in magnetic standard configuration, (top), the divertor components (target plate in grey, baffles in yellow, toroidal closure in cyan) together with confined island remnants (middle) and the complete structure of plasma-facing components with steel panels in terracotta, heat shield in purple and the U-port highlighted (bottom)
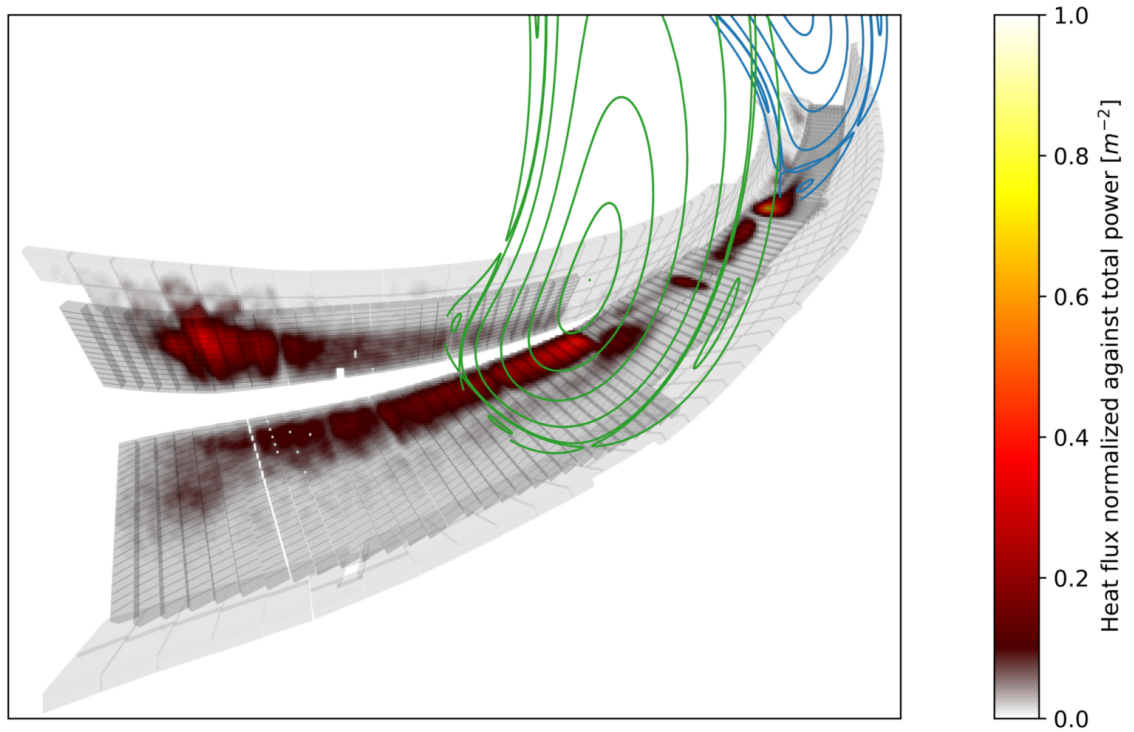
Figure 2: Overview of a single divertor half-module with divertor geometry indicated in grey, magnetic topology for standard $5/5$ configuration overlaid as green and blue in two toroidal cross-section and the simulated heat load distribution (normalized to total power) for $D_{\perp} = 1\,\mathrm{m^2\,s^{-1}}$ overlaid on top of the divertor geometry
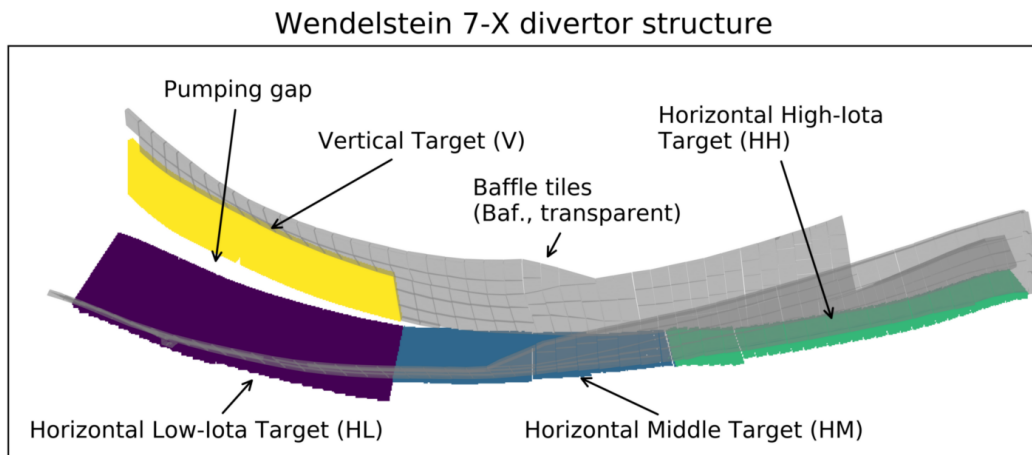

Figure 3: PFC structure of the Wendelstein 7-X divertor system, including the structure of the divertor target plate

3 Setup of the heat load study

3.1 Equilibrium calculation

The magnetic equilibria presented in this paper were calculated using the HINT code (please refer to [12] for a typical application to Stellarator plasmas). HINT is a real-space 3D equilibrium code that directly calculates the equilibrium magnetic field. This operational principle is similar to the full field MHD codes PIES [19] and SIESTA [20]. However, it differs significantly from VMEC and related codes, which calculate the equilibrium assuming a set of nested flux surfaces. This approach allows HINT to incorporate islands and open field lines into its calculation. However, the full 3D representation comes at the cost of significantly increased runtime and memory usage of the code, making a supercomputer an absolute requirement for its execution and imposing computational budgeting constraints on equilibrium studies.

The following paragraphs give a summaric overview over the design underlying the HINT code. For a full overview, please refer to [13]. In HINT, the equilibrium is obtained by explicit time integration of modified single-fluid MHD time-evolution equations (please note that the code supports additional terms unused in this study):

$$
\begin{aligned}
\frac{d\vec{B}}{dt} &= f_{\text{coil}} \cdot \left(\vec{\nabla} \times \vec{E} + \kappa \vec{\nabla} \left(\vec{\nabla} \cdot \vec{B} \right) \right) \\
&= f_{\text{coil}} \cdot \left(\vec{\nabla} \times \left(\vec{v} \times \vec{B} - \eta \vec{j} \right) + \kappa \vec{\nabla} \left(\vec{\nabla} \cdot \vec{B} \right) \right) \\
\rho \frac{d\vec{v}}{dt} &= -\rho \vec{v} \cdot \left(\vec{\nabla} \vec{v} \right) - \vec{\nabla} p + \nu_0 \Delta \vec{v} + \vec{j} \times \vec{B} \\
\vec{j} &= \vec{\nabla} \times \vec{B}
\end{aligned}
$$

Here, η and ν_0 are parameters for resistivity and viscosity, respectively. The term $\kappa \vec{\nabla} \left(\vec{\nabla} \cdot \vec{B} \right)$ is a numerical stabilization term annihilating magnetic monopoles that might arise due to numerical errors. f_{coil} is an indicator function which is 1 outside the coils and 0 inside, prohibiting current evolution inside the region occupied by the superconducting coils. Since the coils are made from superconducting material, the field lines generated by the plasma do not penetrate deeply into the coil material. As the magnetic field is - in stellarators - dominated by the vacuum field, η can be set to be unphysically large in order to match the convergence rates of $\vec{B}$ and $\vec{v}$. The viscosity ν_0 is mainly artificial and exists to dampen oscillations in the early steps of the simulation (where the pressure gradients are not yet balanced by the current). Please note, that, while such a setting does not significantly affect the equilibrium magnetic field, the magnitude of $\vec{v}$ in the will exceed the physical magnitude, to match the higher electric field due to the increased resistivity.

HINT integrates these equations using a high-order explicit Runge-Kutta scheme. The spatial discretization is a 4th-order finite-difference scheme over a cylindrical grid. The code supports periodic boundary conditions along the toroidal direction by specifying the simulated device's toroidal symmetry. In order to maintain a 3D pressure distribution consistent with the magnetic field topology, the pressure field is averaged over a finite distance along the field lines. Since this averaging process is performed repeatedly (alternating with a fixed number of magnetic relaxation iterations), the integration length along the field line can be chosen far shorter than the average connection length in the edge region. Since the averaging process dilutes the pressure profile over time, the pressure is periodically reset to a specified flux function. This presents a challenge to the numerical scheme: As the topology is not limited to nested flux surfaces, there is no flux coordinate available to derive the pressure profile from. To overcome this problem, HINT relies on the constant pressure surfaces as pseudo flux surfaces. The magnetic flux value used for the profile is the integrated magnetic flux inside these surfaces. This scheme produces acceptable results but requires an initial 3D magnetic flux profile to initialize the pressure distribution calculation.

In this study, the response to the increase in plasma pressure is studied for three different magnetic configurations. These configurations mainly differ from each other by the value of the edge rotational transform, which is either $5/4$ (4 toroidally connected edge islands, "high-iota"), $5/5$ (5 individual edge islands, each in a separate flux tube, "standard") and $5/6$ (6 toroidally connected edge islands, "low-iota"). Please refer to [21] for a more detailed description of the magnetic configuration space. The magnetic configurations are based on the ideal CAD coils of W7-X. This differs from the device's experimental conditions, where the coils are flattened by Lorentz forces exerted on the current carriers in the strong external fields. This results in a small change of the edge rotational transform, which is compensated by a modification of the planar coil currents (in the order of a few $100\,\text{A}$, configuration dependent and small compared to the dynamic range of the non-planar coil current, which is in the order of $\pm 10\,\text{kA}$) during operation. The MHD calculations were performed on a 5-fold toroidally symmetric cylindrical (around the z axis) grid with a total of $n_r \times n_z \times n_\phi = 256 \times 256 \times 128 = 8388608$ grid points, which is sufficient to resolve the structure of the pressure profile and accurately capture its derivatives, as well as resolve the coarse structure of the edge islands. The toroidally symmetric setup was chosen for the simulations both to conserve computing resources (with the chosen scheme already topping out at about $5000\,\text{CPUh}$) and to avoid additional free parameters from the parametrization of magnetic field asymmetries. The pressure profiles for HINT were specified in terms of normalized toroidal flux s. Synthetic pressure profiles of the form $p \propto (1-s)^\alpha$ (with α being a free parameter)

were assumed for this study, which provided an acceptable fit to pressure profiles derived from Thomson scattering (T_e, n_e)[22, 23, 24] and XICS (T_I)[25, 26] measurements. For these profiles, the peaking factor (the ratio between central plasma beta and volume-averaged plasma beta) can be approximated as $f_p \approx \alpha + 1$. For equilibria with toroidal plasma current, a peaked current profile of $I \propto (1-s)^2$ was assumed. The pressure relaxation step of the HINT code requires a cutoff length for its field line averaging calculation. Both for performance reasons and to mimic the effects of parallel diffusion in the edge region, we chose a short averaging length of $L_C = 10\,\mathrm{m}$, which is below the typical connection length (which is in the range of $100\,\mathrm{m}$ to $500\,\mathrm{m}$) and the machine circumference (which is approximately $35\,\mathrm{m}$). The short averaging length is compensated by performing a larger number of macrocycles. The initial estimates for the 3D magnetic flux function were obtained from VMEC runs in the Wendelstein 7-X VMEC reference equilibrium database [27]. Points outside the VMEC LCFS were geometrically extrapolated from the magnetic axis and the LCFS. The simulations were performed on the JURECA supercomputer [28].

3.2 Anisotropic Diffusion

To estimate the heat loads on the divertor plate, we implemented an anisotropic heat diffusion model. Heat packets are seeded on a nonresonant magnetic surface 1mm inside the last closed surface. In all Poincaré plots, these seeding surfaces are indicated in red. The heat packets then undergo alternating steps between an parallel random walk step, which was implemented via tracing along the field line, and an isotropic random walk step. The parallel tracing length $l_\parallel$ (where positive sign is in field direction and negative sign against) and isotropic displacement Δx are sampled according to the following rules:

$$p\left(l_\parallel = k\right) = \left(2\pi\sigma_\parallel^2\right)^{-1/2} \exp\left(-\frac{k^2}{2\sigma_\parallel^2}\right)$$

$$p\left(\Delta x = \vec{k}\right) = \left(2\pi\sigma_{\mathrm{iso}}^2\right)^{-3/2} \exp\left(-\frac{\left|\vec{k}\right|^2}{2\sigma_{\mathrm{iso}}^2}\right)$$

$$\sigma_{\mathrm{iso}} = \sigma_\parallel \sqrt{\frac{D}{D_\parallel}}$$

When either tracing or displacement passes through a divertor mesh element, the particle trajectory is terminated and the strike point is recorded. This gives a Monte-Carlo model for standard anisotropic heat diffusion of an energy density E

$$\frac{dE}{dt} = -\nabla \cdot \vec{J_E} + f_{\mathrm{heating}} \tag{1}$$

$$\vec{J_E} = -D\nabla E - D_\parallel \vec{b}\left(\vec{b}\cdot\nabla E\right) \tag{2}$$
$$\Rightarrow$$
$$\frac{dE}{dt} = \nabla \cdot \left(D\nabla E + D_\parallel \vec{b}\left(\vec{b}\cdot\nabla E\right)\right) + f_{\mathrm{heating}} \tag{3}$$
$$\vec{b} = \vec{B}/|\vec{B}|$$

with an anisotropic axis $\vec{b}$ derived from the magnetic field $\vec{B}$, scalar diffusion coefficients D and $D_\parallel$ and a heating function f_{heating}, which in this case is a distribution concentrated on the magnetic surface in which particles are seeded. The energy flow in equation 2 consists of an isotropic diffusion component (flow against the energy density gradient) and a, usually larger, anisotropic diffusion against gradient in magnetic field direction. Together with the energy balance equation 1, one can obtain the anisotropic diffusion process described by equation 3. The boundary condition for this model is a Dirichlet boundary condition ($E = 0$) on the divertor mesh. The strike point distribution (samples using the above Monte-Carlo routines) yields the power loads impacting onto the divertor surfaces, normalized against the total heating power (given by the sum of the - in this case even - test packet weights). Due to this normalization, as well as the linearity of the simulated model, the model is invariant under common rescaling of D and $D_\parallel$. Therefore, only the diffusion coefficient ratio $D/D_\parallel$ between the anisotropic and parallel diffusion coefficients is of physical relevance. This is also reflected in the model implementation, in which the anisotropic step size is derived from the parallel step size and the diffusion coefficient ratio. Compared to the heat transport model in EMC3-EIRENE [29], this model assumes fixed diffusivity ratio $D/D_\parallel$ (which corresponds to the terms $\chi_\square n_\square / \kappa_\square$ in [29, equations 3 and 4], where the box is a placeholder for electron and ion species) and neglects density gradient effects as well as the parallel convection term. Introducing these terms would make the simulation nonlinear and would lead towards an inferior implementation of existing scientific codes.

The remaining parameter for this model is the choice of the parallel step standard deviation $\sigma_\parallel$. This choice is strongly coupled with a computational tradeoff: The average distance between a particle and its seeding point in a random walk scales as $\mathcal{O}\left(\sqrt{n}\right)$ with the step count n. Therefore, the computation time for a trajectory required to cross a specific distance L scales with $\mathcal{O}\left(L^2/\sigma_\parallel\right)$ (as the number of steps scales with $\mathcal{O}\left(\left(L/\sigma_\parallel\right)^2\right)$ and their cost scales with $\mathcal{O}\left(\sigma_\parallel\right)$). Here, we chose a special strategy to circumvent this problem. Small scale phenomena are most relevant near the X-point of the magnetic topology, which is near the seeding region, while downstream phenomena are based on heat exchange between field lines over longer spatial scales (as the connection lengths are above $100\,\mathrm{m}$). We therefore choose to grow $\sigma_\parallel$ linearly with the number of steps (and adjust σ_{iso} accordingly). This combines high spatial accuracy in

the upstream region with acceptable computation times (around 300 core hours per simulation for 10^6 starting points).

We would like to stress that this model only gives a simplified view on heat transport in magnetic confinement plasmas. Particularly, a full simulation would require at least a two fluid treatment (due to the different diffusivities between electrons and ions), a more rigorous treatment of scattering processes, and the consideration of plasma potential- and boundary sheath-effects. These points would mandate nonlinear simulations, which are both more time consuming and substantially more difficult to implement in a Monte-Carlo setting. Instead of a complete treatment of the heat transport, this model aims to give a tool for studying the trends related to an increase in plasma beta. The baseline to extrapolate from should be preferentially based on experimental data or more sophisticated transport models like EMC3. The main issue with nonlinear transport models (such as EMC3-EIRENE) is that the nonlinearity requires a larger number of iterations. To mitigate this issue, EMC3-EIRENE in particular uses a grid to accelerate field line tracing computations for parallel transport calculation. These grids are dependent on the background magnetic field. Unfortunately, we are not aware of a method to automatically generate batches of sufficient quality grids without human intervention, so we had to rely on a linear model without such acceleration techniques.

3.2.1 Influence of the diffusivity ratio

The ratio between perpendicular / isotropic diffusion and parallel diffusion plays a major role in the behavior of the obtained heat load model. As can be seen in figure 4, the heat load distributions at different diffusion coefficients differ in their qualitative structure. When the perpendicular diffusion is small ($D/D_\parallel \approx 10^{-7}$), virtually all heat flows directly along the island separatrix from the core onto the divertor plates. In this case, most of the heat is deposited into the main strike line. As the perpendicular component of the diffusivity is increased, two effects are visible: The first is an increase in the strike pattern width (it can be seen that the reduction in peak flux is disproportionately large when compared to the reduction in total load). Another effect is the increase of heat flow onto plasma-facing components shadowed by impact targets of the primary strike line. This first affects previously unloaded divertor target components such as the high-iota section (when operating in standard configuration). As perpendicular diffusion becomes more relevant, however, it also directs heat flows away from the divertor onto other plasma-facing components.

Since the heat load distribution depends strongly on the choice of the anisotropic diffusivity ratio, a comparison is only valid for a specifically chosen value. However, as it is the only physically relevant free parameter,

matching this parameter against the experimental observations does not present a substantial issue, as the number of observed degrees of freedom is rather large. For comparison with experiment, we chose to focus on the range between 10^{-6} and 10^{-7}, which appears to be roughly in line with the IR camera observations of the divertor heat loads.

3.3 Synthetic Camera for Heat Flux Measurements

The dataset resulting from the field line-diffusion simulation is a set of point clouds and a rough estimate of the heat load distribution binned over the triangles of the divertor geometry mesh. In order to determine more precise heat-flux estimates, the point-cloud is usually first mapped into a geometry reference space with known metric and then binned. The resulting 2D images are then again transformed into a virtual camera view. This process requires a substantial amount of manual setup for unrolling of the individual geometries and is challenging to extend to the whole machine due to its complex, partially non-manifold geometry. In this work, we use the pixels of the synthetic camera itself as the binning grid. The normalized heat-fluxes can be computed from the normalized strike-point distribution over the pixels via division by the surface area observed by the individual pixels. This information can be computed in advance. To account for statistical fluctuations and distortions from the projection transformation, the virtual heat load images are convolved with a Gaussian filter kernel. The radius of the gaussian kernel is chosen locally from the inverse area covered by the pixel (so that pixels already covering large areas have a weaker low-pass filtering).

4 Assessment of configurations for high-beta operation

It is challenging to make a configuration-independent general statement on how the magnetic topology responds to the transition from vacuum to finite-beta scenarios. All investigated configurations exhibit unique response characteristics, both in their magnetic topologies and in the associated divertor heat loads. Therefore, the results of the simulation study are discussed on a per-configuration basis. The peak loads, as well as the calculated load distribution between plasma-facing components, are presented in figures 5 and 6, respectively. As the main area of interest is the effect of changing overall beta, we chose to restrict these figures to the cases with a pressure profile linear in normalized toroidal flux (roughly parabolic in minor radius) $p \propto 1 - s$. For a full overview of the simulations (which also include some cases with toroidal current not discussed in the main work), we would encourage the reader to look into ta-
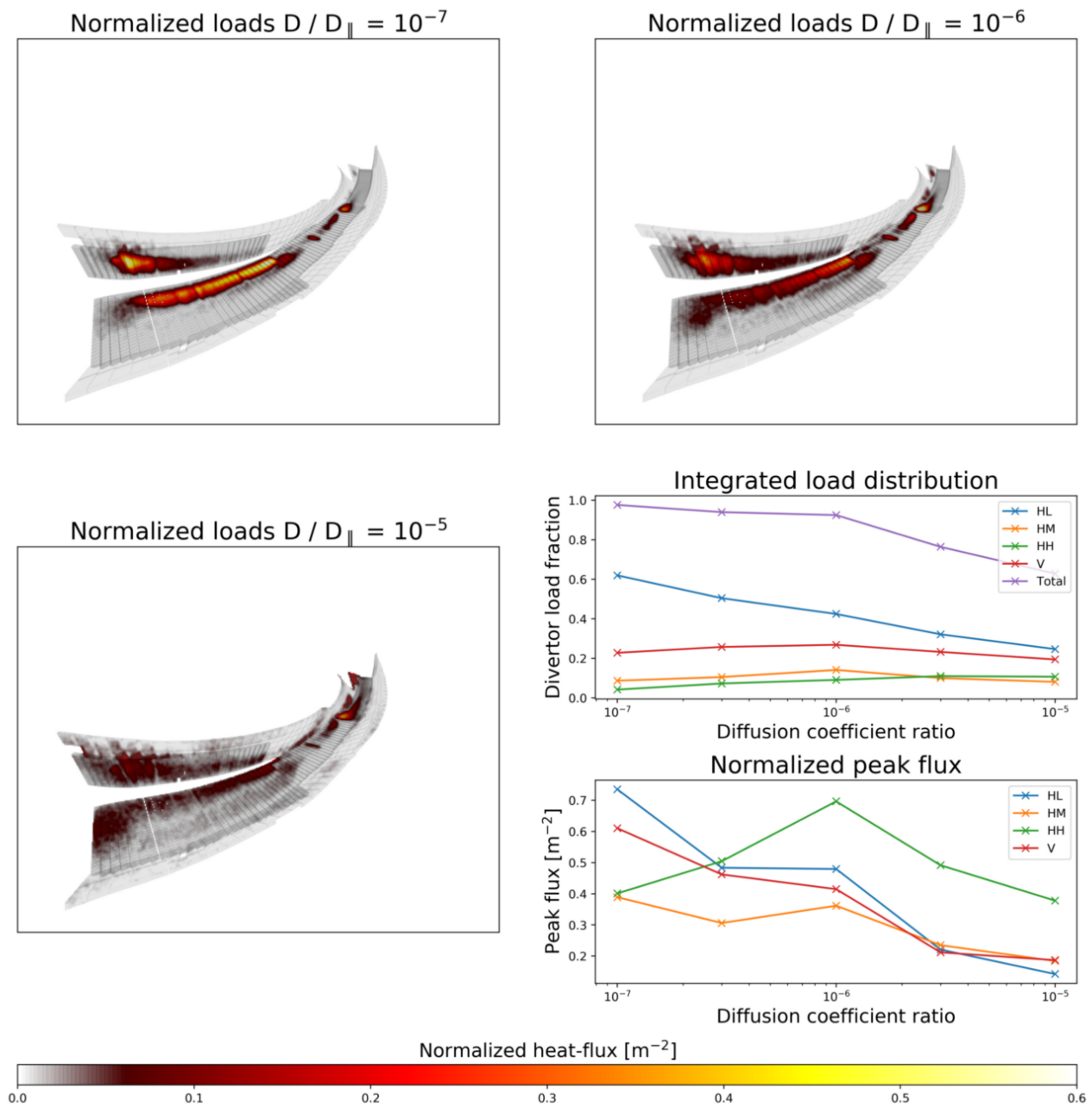
Figure 4: Heat load distribution for vacuum field standard configuration at different diffusion coefficients.

ble 1.

4.1 Standard configuration (5/5)

Figure 7 shows the influence of overall plasma beta on the standard configuration's edge magnetic field structure. As on-axis plasma beta increases, the separatrix of the island chain begins to show stochastization. However, even at high plasma beta, a structured set of nested flux surfaces remains intact both surrounding, as well as in the interior of the island chain. The outboard stochastic side of the island intersects slightly with the U-port in the triangular plane (see figure 1 for location of these ports). However, no significant heat-flux was visible on this port in the $p \propto s$ cases even at 5% central beta. At higher plasma beta, the edge islands near the divertor plates are moved slightly inwards (towards the center of the machine, not the magnetic axis). This changes the connection structure of the island. Where in the vacuum field only the bottom left part of the separatrix connected directly to the divertor, the shift of the island causes first a connection to the vertical target plate and then, at higher plasma beta, a connection to the outboard side of the divertor island. The heat load distribution on the divertor (shown in figure 8) reflects this behavior directly, forming first an additional strike-line on the vertical target plate and then a secondary (albeit weak) strike-line on the horizontal target. While peak heat loads vary in the high-load areas (mostly HL and V), the load-limiting middle section appears to be subjected to a constant normalized peak-flux of $0.4\,\mathrm{m}^{-2}$, which slightly decreases with increasing plasma beta to about $0.3\,\mathrm{m}^{-2}$. This limits the convective divertor power to about $2\,\mathrm{MW}$ (see table 1 in the appendix for a more detailed investigation).

The area of the stochastic region in the edge does not appear to have a significant dependence on volume averaged beta at fixed central beta (as shown in the profile scan in figure 9). However, the separatrix shape and the position of the island's O-point react to the change in profile like they react to the change in central beta. This indicates that the primary driver for the island shaping effect is the central pressure, while the stochastization depends on volume integrated pressure.

4.2 High-Iota configuration (5/4)

In the $\iota = {}^{n}/m = {}^{5}/4$ configuration, the edge islands form a single flux tube winding helically around the plasma core. The vacuum configuration features no nested flux surfaces outside of the edge islands. Therefore, these islands are highly susceptible to stochastization due to the lack of nested magnetic surfaces outside the island-region [7, 17]. As figure 10 shows, the nested magnetic surface structure of the islands is lost with increasing beta. This can be attributed to the growth of the edge islands with increasing beta. As the edge islands grow, the overlap

with the outer stochastic region increases, which leads to a loss of the islands' nested flux surface structure. Additionally, higher-order resonances near the island separatrix also contribute to the increase in stochastization. However, the connection-length distribution reveals a deterministic lobe-like structure in the chaotic Poincaré-map. It can also be seen from both figures that, although the microscopic edge structure becomes increasingly chaotic at high beta, the O- and X-point position (which can be estimated from the connection-length distribution, e.g. in figure 10 row 3 as the intersection points of the jumps in connection-length for the O-point and the intersection point of the lobe-structures for the X-point) of the lowest-mode perturbation remains relatively stable.

Nonetheless, the distortion of the separatrix due to the stochastization has visible effects on the edge magnetic field topology. In the low-beta cases, the separatrix of the island chain passes the vertical target nearly tangentially by less than 1 cm. As plasma beta increases, this part of the separatrix retracts from the vertical target, and the heat flux is redistributed toward the tail of the horizontal divertor plate (see figure 11), balancing out the divertor heat load on the high-iota target section and reducing the loads on the vertical target. The strike-line width itself, however, appears to be mostly unaffected by the stochastization effects. The stochastization of the magnetic island region also appears to have a dependency on the pressure profile at fixed central beta, but the magnetic islands are not fully recovered in the cases with high central plasma beta ($\beta_{\mathbf{ax}} = 5\%$) and low volume-averaged beta ($\beta_{\mathbf{vol}} = 0.5\%$) (figure 12).

As seen in table 1, the high-iota configuration is subject to the highest peak heat-fluxes (at above $1.5\,\mathrm{m}^{-2}$) onto the divertor target plate. In this situation, the heat load limit on the high-iota tail (HH) approaches values near the limit imposed by the middle section (HM), although calculations still indicate the middle section to be the load-limiting factor. The exact limitation scenario is sensitive to the diffusion coefficients, as an increase of cross-field diffusivity in the edge both defocuses the heat loads on the high-iota tail and increases the indirect (supplied by diffusion) heat-flow onto the middle section. Similarly sensitive to the diffusivity is the limitation imposed by the baffle heat loads. As can be seen in figure 13, this is mainly related to a set of baffle tiles sitting right above the vertical target. Since the closeby passing separatrix recedes with increasing plasma beta, this area is progressively unloaded as plasma pressure increases. This effect is, however, substantially less pronounced at high edge diffusivity.

At high plasma beta, the outboard side of the triangular-plane cross-section (figure 10, middle row) starts - due to the stochastization - to overlap with the plasma-facing components. As can be seen in figure 14, this can lead to the deposition of a substantial amount
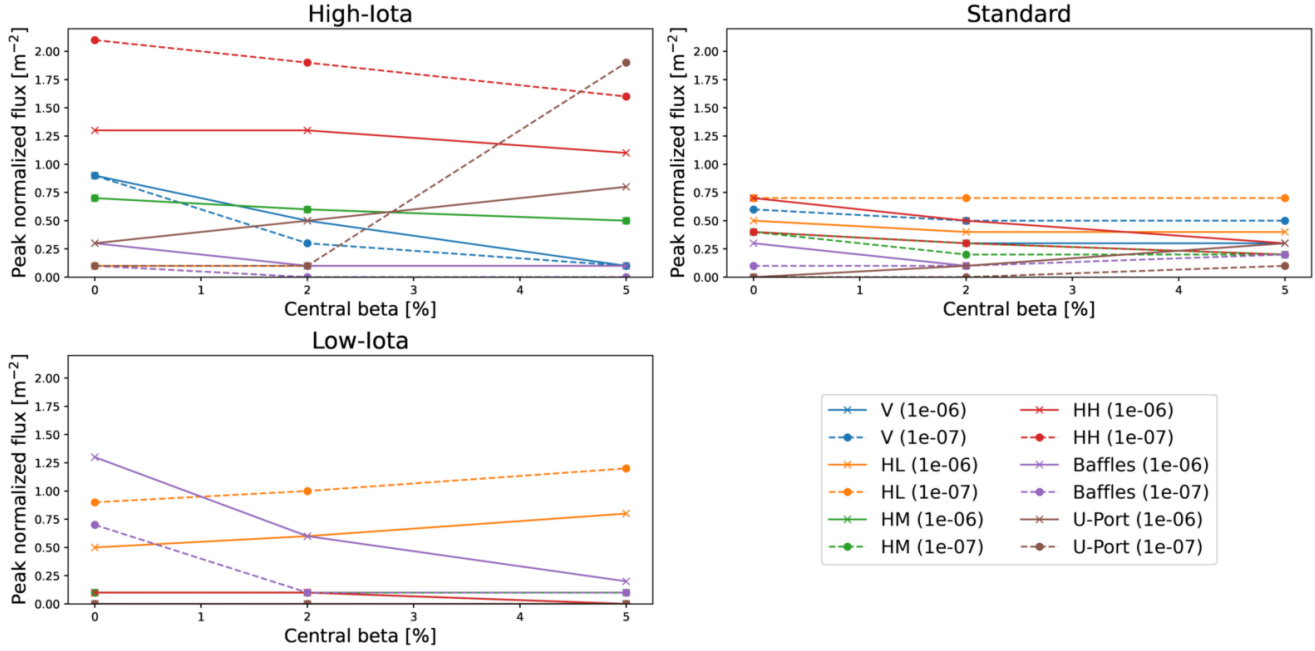
Figure 5: Peak heat loads on the plasma-facing components for different configurations as a dependency of central plasma beta. Line colors indicate the target component. Solid lines indicate an assumed diffusivity ratio $D/D_{\parallel} = 10^{-6}$, while dashes lines indicate a value of 10^{-7}.
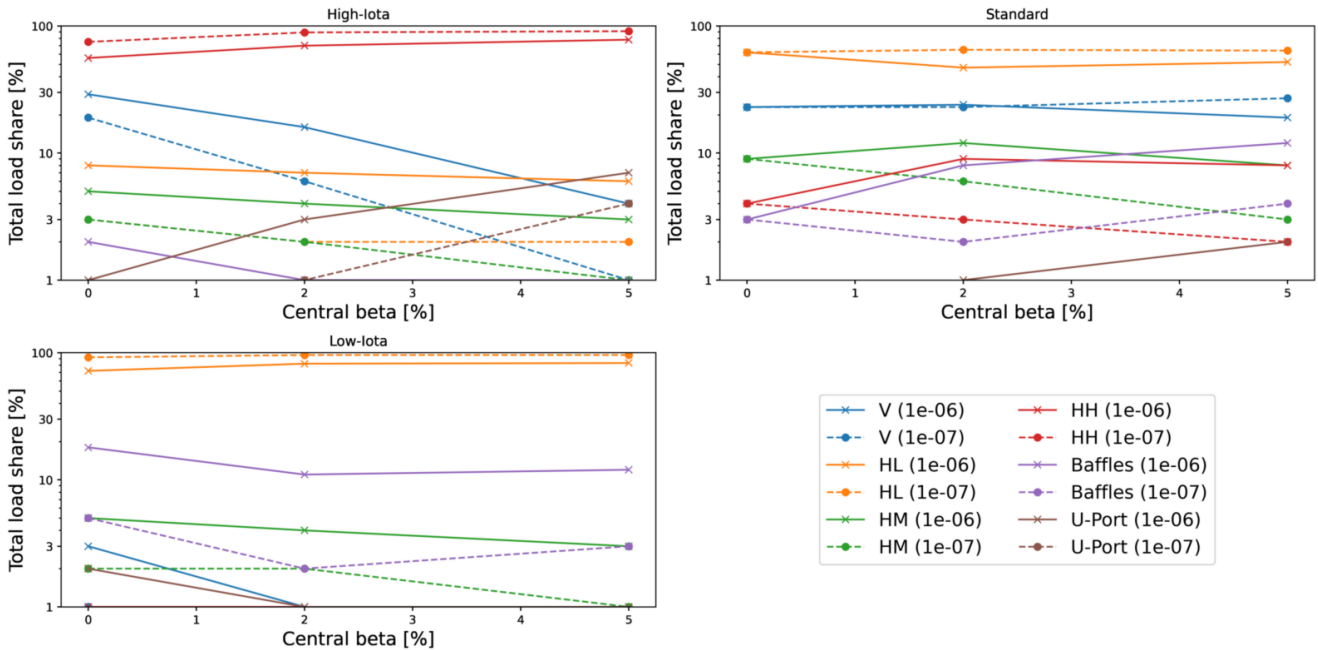

Figure 6: Integrated load distributions on the plasma-facing components for different configurations as a dependency of central plasma beta. Line colors indicate the target component. Solid lines indicate an assumed diffusivity ratio $D/D_{\parallel} = 10^{-6}$, while dashes lines indicate a value of 10^{-7}. Fractions are presented on log-scale to better capture the lower end of the range.
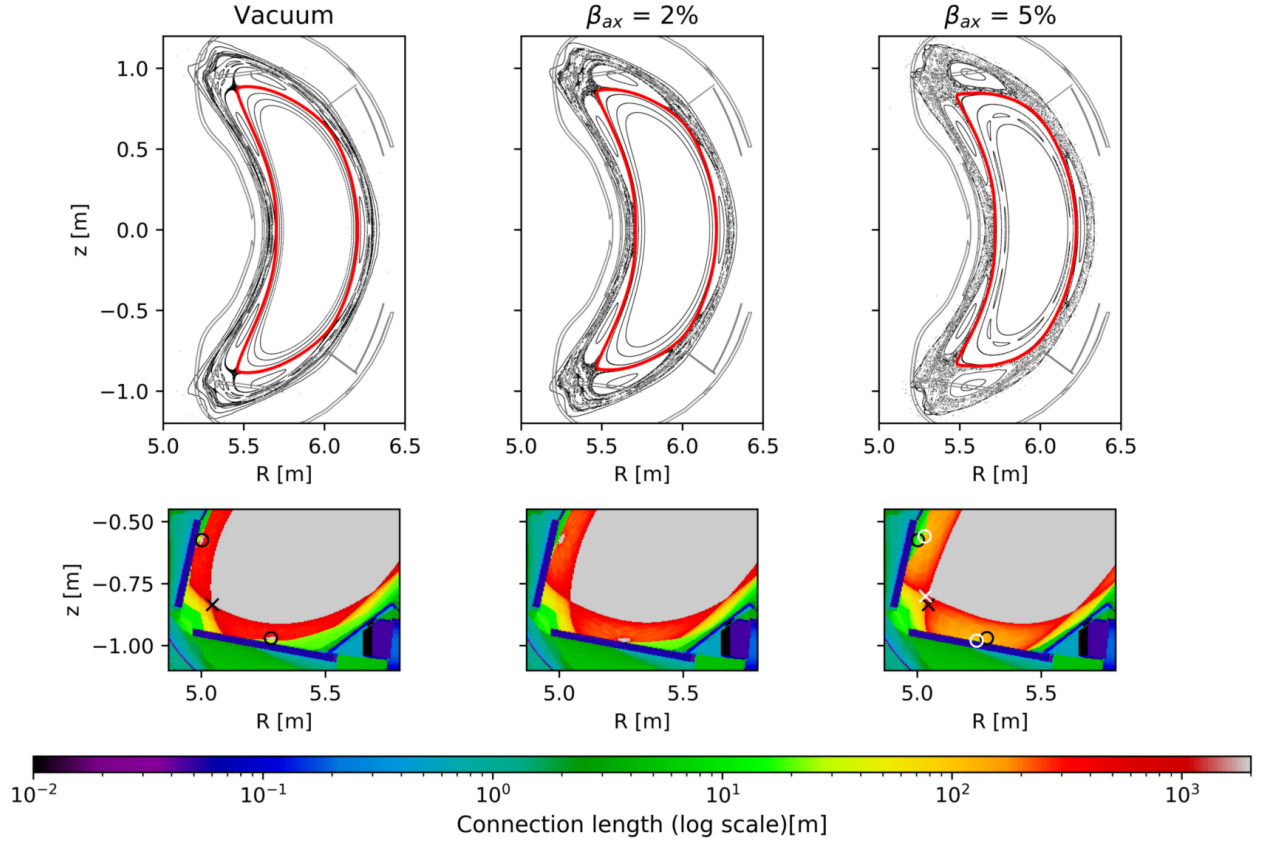
Figure 7: : Plasma response in standard configuration at fixed pressure profile ($p \propto 1 - s$) to changes in axial beta for vacuum case (left), $\beta_{ax} = 2\%$ (middle) and $\beta_{ax} = 5\%$ (right). Poincaré-maps are shown in the $\phi = 0°$ plane (bean-plane), while connection-length distributions are plotted at the front (low-iota) end of the divertor plate. Flux surfaces for seeding heat load packets are marked in red. Low-beta X- and O-points are marked in black, while X- and O-points for the high-beta configuration are marked in white.
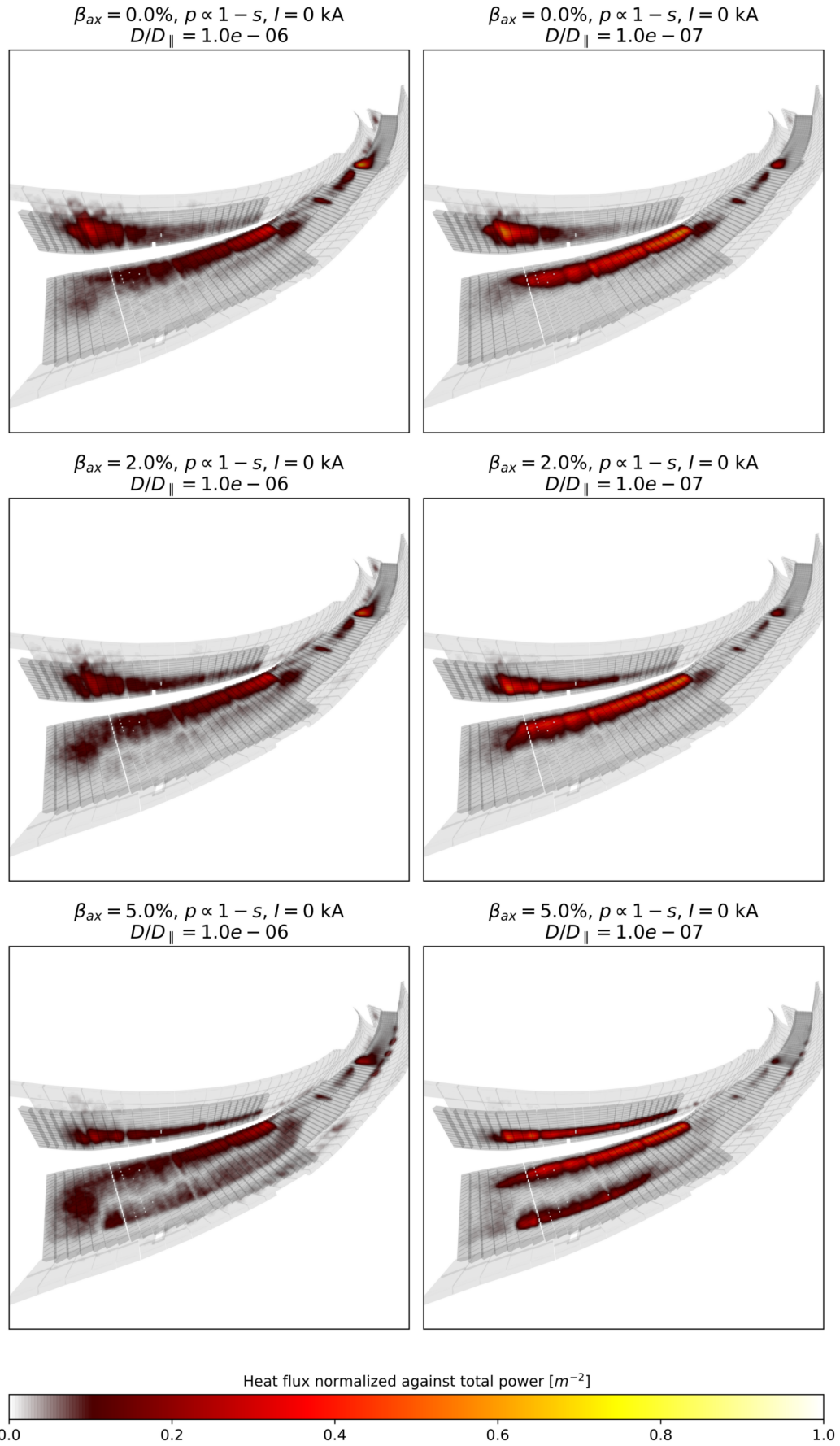
Figure 8: Changes in divertor heat loads in standard configuration with increasing axial beta and toroidal plasma current.
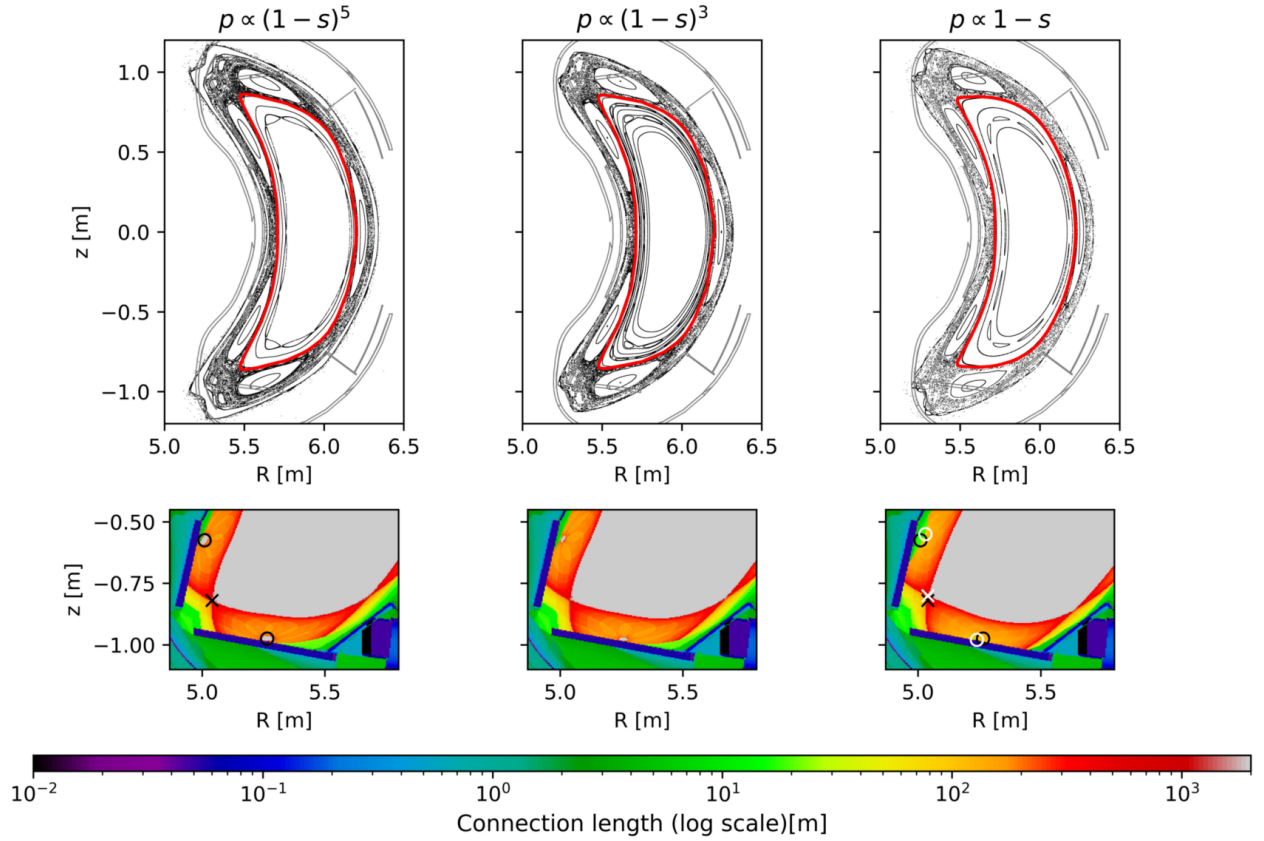
Figure 9: : Plasma response in standard configuration at fixed axial beta ($\beta_{\mathrm{ax}} = 5\%$) to changes in pressure profile shape, with $p \propto (1-s)^5$ (left), $p \propto (1-s)^3$ (center) and $p \propto 1 - s$ (right). Poincaré-maps are shown in the $\phi = 0°$ plane (bean-plane), while connection-length distributions are plotted at the front (low-iota) end of the divertor plate. Flux surfaces for seeding heat load packets are marked in red. Low-beta X- and O-points are marked in black, while X- and O-points for the high-beta configuration are marked in white.
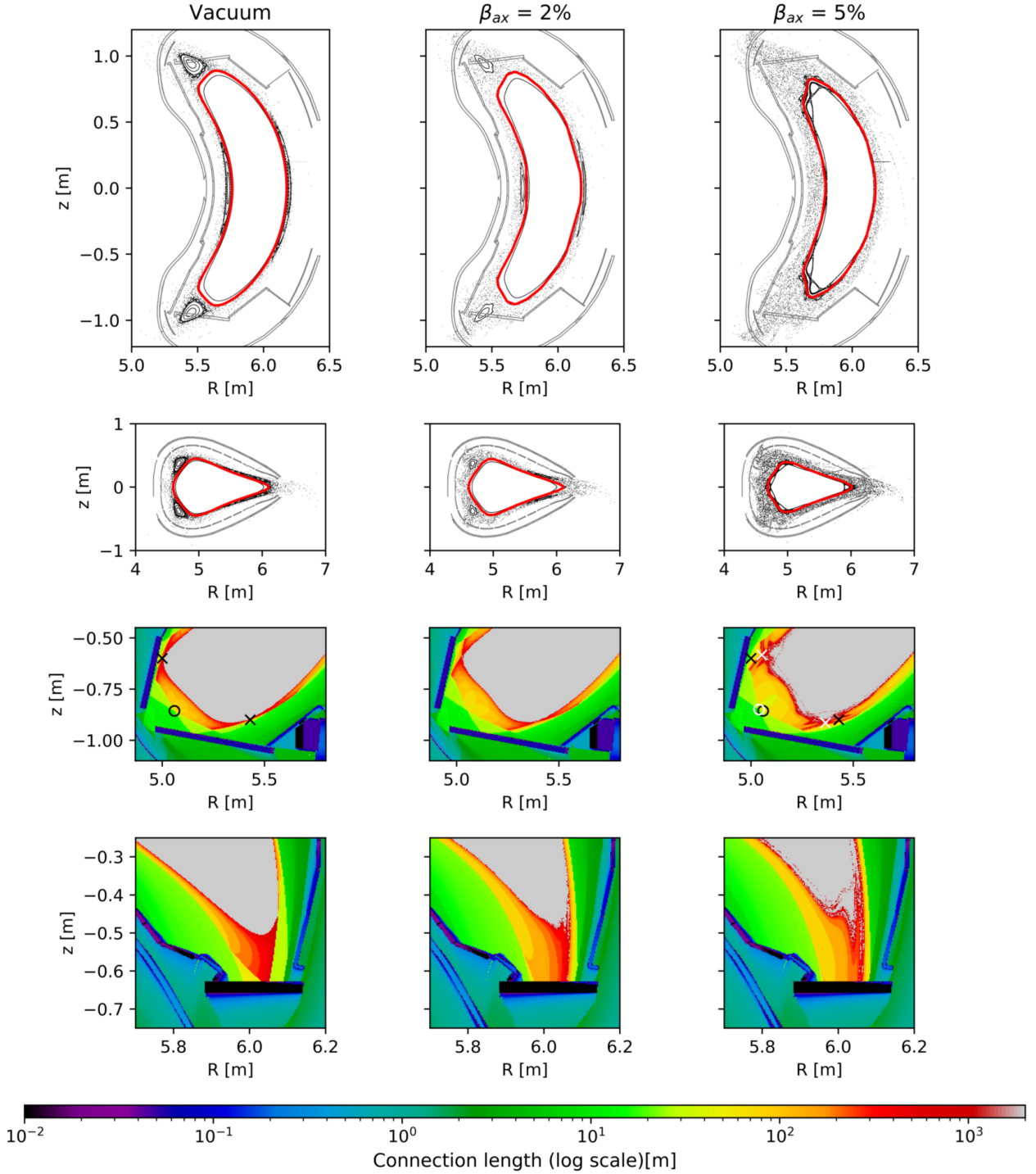
13

Figure 10: Plasma response in high-iota configuration at fixed pressure profile ($p \propto 1-s$) to changes in axial beta for vacuum case (left), $\beta_{ax} = 2\%$ (middle) and $\beta_{ax} = 5\%$ (right). Poincaré-maps are shown in the $\phi = 0°$ plane (bean-plane, top) and the $\phi = 180°$ plane (triangular plane, upper middle), while connection-length distributions are plotted at the front (low-iota) end (lower middle) and the back-(high-iota)-end (lowest row) of the divertor plate. Flux surfaces for seeding heat load packets are marked in red.

$\beta_{ax} = 0.0\%,\ p \propto 1 - s,\ I = 0$ kA, $D/D_{\parallel} = 1.0e - 06$

$\beta_{ax} = 2.0\%,\ p \propto 1 - s,\ I = 0$ kA, $D/D_{\parallel} = 1.0e - 06$
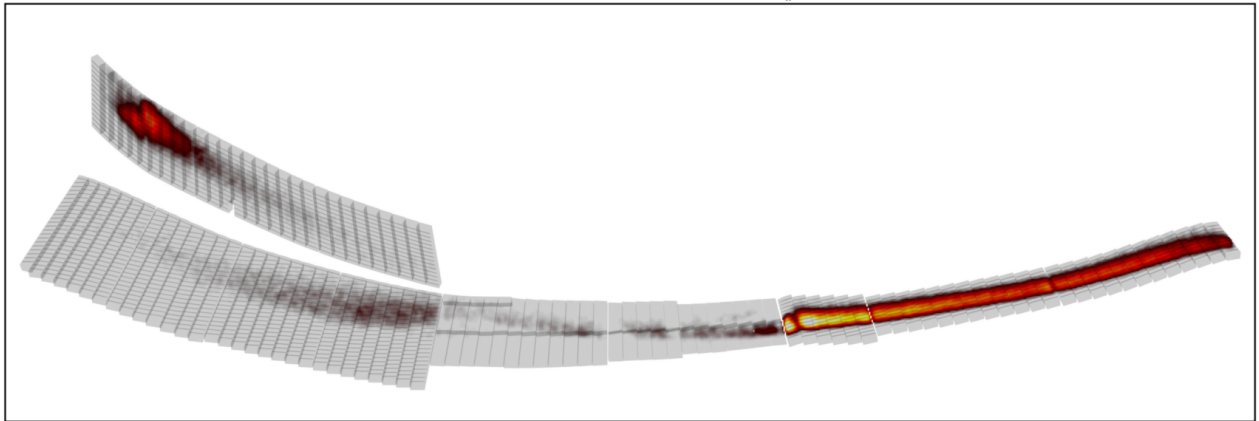
$\beta_{ax} = 5.0\%,\ p \propto 1 - s,\ I = 0$ kA, $D/D_{\parallel} = 1.0e - 06$

Heat flux normalized against total power $[m^{-2}]$

0.0   0.2   0.4   0.6   0.8   1.0

Figure 11: Divertor heat load distributions in high-iota configuration for different central beta values
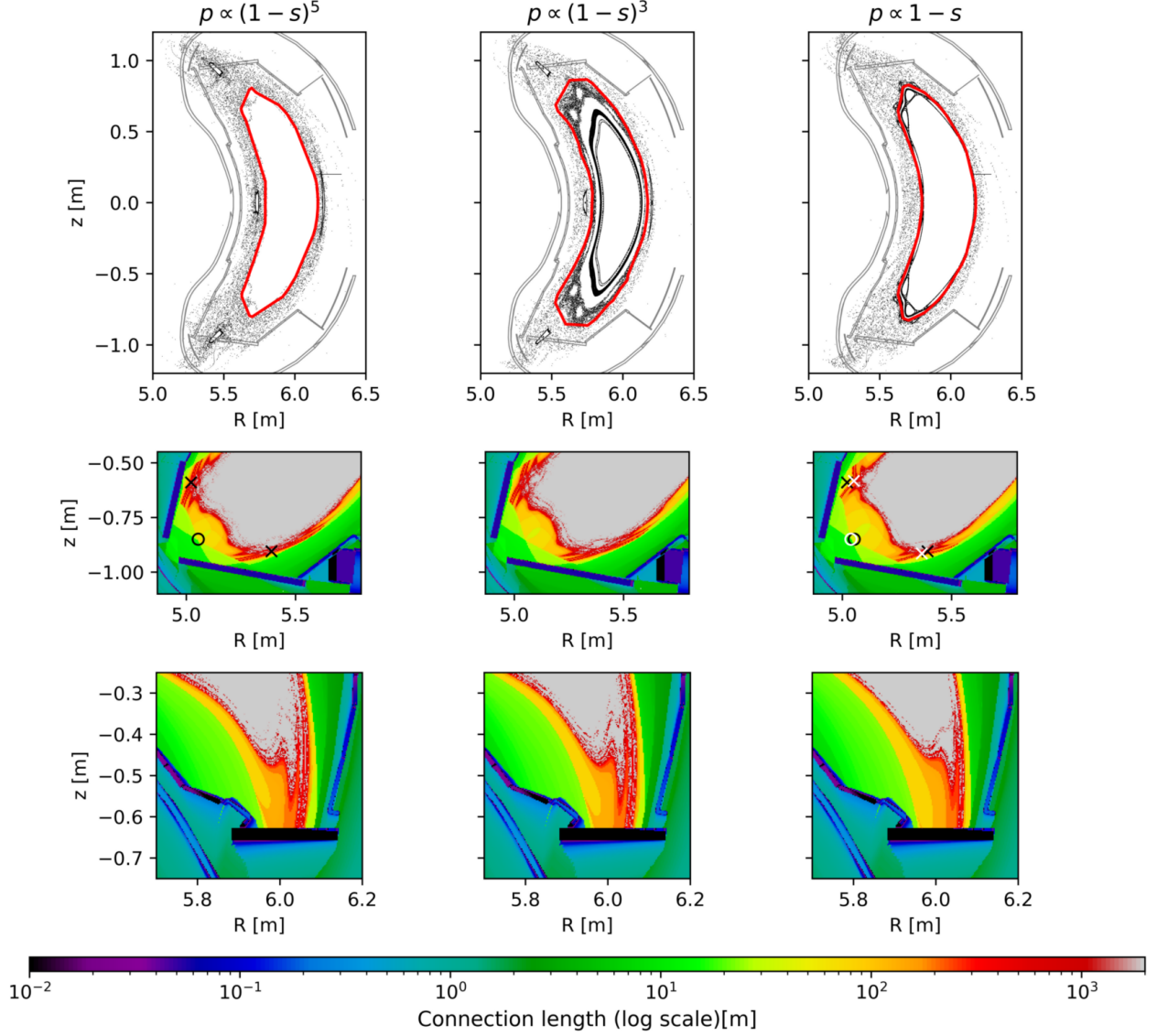
Figure 12: Plasma response in high-iota configuration at fixed axial beta ($\beta_{\mathrm{ax}} = 5\%$) to changes in pressure profile shape, with $p \propto (1-s)^5$ (left), $p \propto (1-s)^3$ (center) and $p \propto 1-s$ (right). Poincaré-maps are shown in the $\phi = 0°$ plane (bean-plane), while connection-length distributions are plotted at the front-(low-iota) end (middle) and the back-(high iota)-end (lower) of the divertor plate. Fl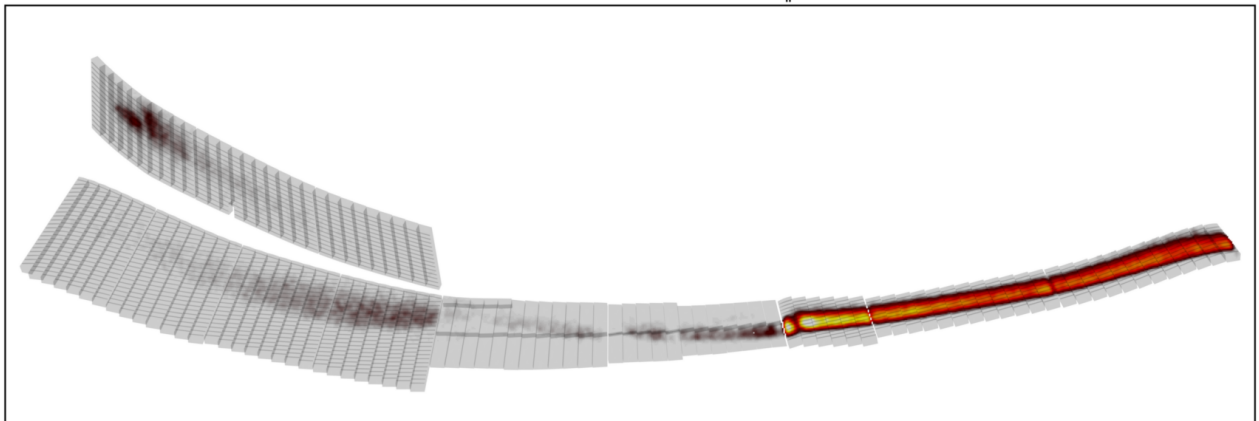ux surfaces for seeding heat load packets are marked in red. Low-beta X- and O-points are marked in black, while X- and O-points for the high-beta configuration are marked in white.

Figure 13: Divertor baffle heat load calculation in high-iota configuration (vacuum field)

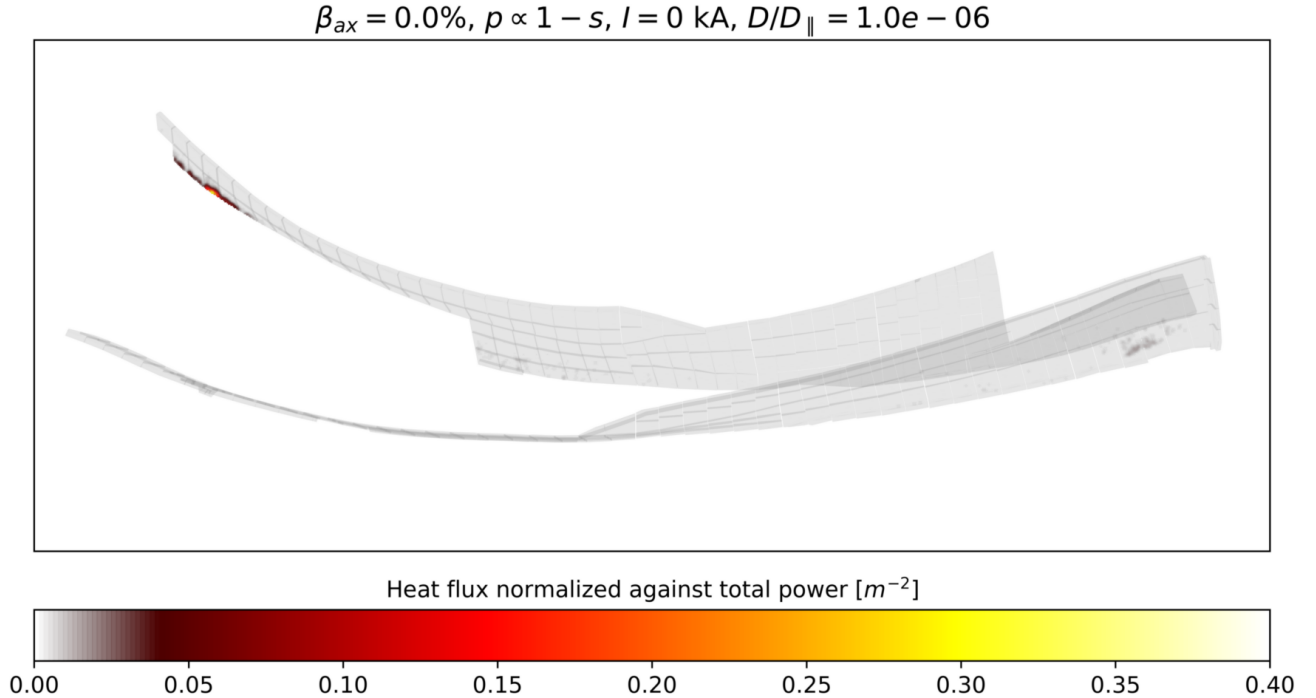of power onto the horizontal port in this plane, with up to 7% of the total heating power being deposited near the five U-ports. A significant share of this power is deposited onto small spots (estimated at about $0.7\,\mathrm{dm}^2$ per spot) at the edge of the port. For steady-state operation, care must be taken in this configuration in high-performance scenarios, as these heat loads could quickly exceed the heat-dissipation ability of the cooling system, thus posing problems for steady-state operation.

4.3 Low-Iota configuration (5/6)

The 5/6 island ("low-iota") configuration also shows topological sensitivity to the plasma beta. As was first reported in [9][1], the phase of the beta-driven 5/6 magnetic field component is opposite to the vacuum field's 5/6 component. The resulting annihilation of the 5/6 island chain (at around 5% plasma beta in this study, see figure 15) is beneficial for operation in standard configuration (as the presence of 5/6 islands in the core would degrade confinement). However, it has a detrimental effect when these islands are used as an island divertor, as discussed in [11]. As the islands shrink in size, the separatrix mostly disconnects from the divertor target plate (figure 15), and the overall magnetic topology changes towards a limiter-like configuration. The profile scan (figure 16) shows very similar behavior to the central beta

scan, indicating that the change in the 5/6 component is probably related to volume averaged beta, with the $\beta_{\mathrm{ax}} = 5\%$ and $\beta_{\mathrm{vol}} = 0.5\%$ ($p \propto (1-s)^5$)-case showing almost the same magnetic topology as the vacuum case.

According to the diffusion simulations, the effect of this transition on the heat flux distribution (figure 17) is quite profound. As the pitch angle of the outer separatrix on the target plate decreases due to the shrinking islands, the wetted area increases at first due to a larger strike-line width. After the transition towards the limiter-like configuration, however, the heat flux is focused into a wide spot in front of the usual strike-line position. This circular structure was already observable in lower-beta experiments and showed a strong up-down asymmetry, which can be attributed to particle drifts in the magnetic field (see [31] for an in-depth discussion of these observations).

Due to the reduction in island width and the resulting transition towards a limiter-like configuration, the outboard baffle tiles near the front of the divertor experience additional heat loads. While the total load on the baffles varies with the volume-averaged beta, the peak normalized heat-flux density is at least $0.1 m^{-2}$ in almost all of the scenarios (see table 1). As the circular divertor heat pattern lies on the same flux surface as the baffle hotspots, particle drift effects might create similar up-down asymmetries in heat-flux intensity here.

It should be noted that the islands disappear due to a fairly precise cancellation of the plasma-driven- and vacuum magnetic field component. The island return at

---

[1] This initial work relied on a preliminary version of the planned W7-X coil set, which was changed afterwards. The same effect was then confirmed for the finalized coils in [30] and [17]
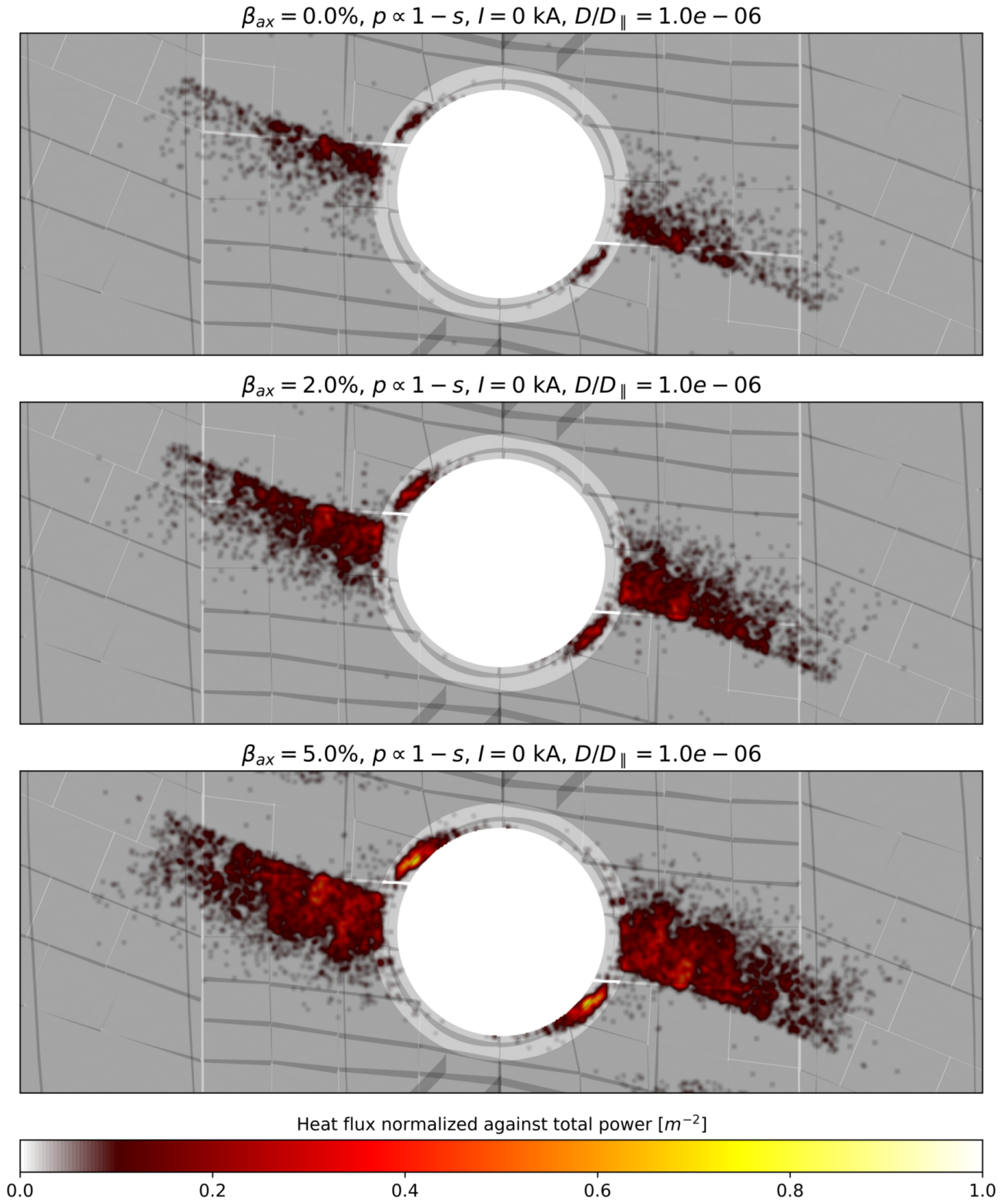
Figure 14: Heat-flux distributions on the outer U-port in high-iota configuration for a vacuum-field calculation (top), a $\beta_{\mathrm{ax}} = 5\%, \beta_{\mathrm{vol}} = 1.25\%$ case (middle) and a $\beta_{\mathrm{ax}} = 5\%, \beta_{\mathrm{vol}} = 2.5\%$ case (bottom)
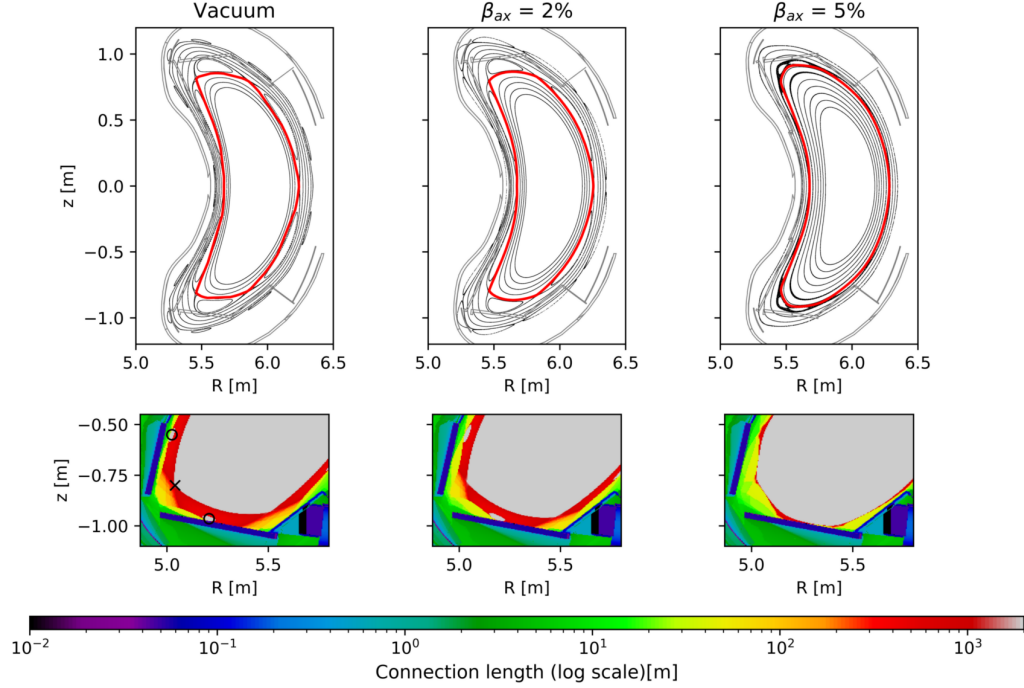
Figure 15: Plasma response in standard configuration at fixed pressure profile ($p \propto 1 - s$) to changes in axial beta for vacuum case (left), $\beta_{ax} = 2\%$ (middle) and $\beta_{ax} = 5\%$ (right). Poincaré-maps are shown in the $\phi = 0°$ plane (bean-plane), while connection-length distributions are plotted at the front (low-iota) end of the divertor plate. Flux surfaces for seeding heat load packets are marked in red. Low-beta X- and O-points are marked in black.
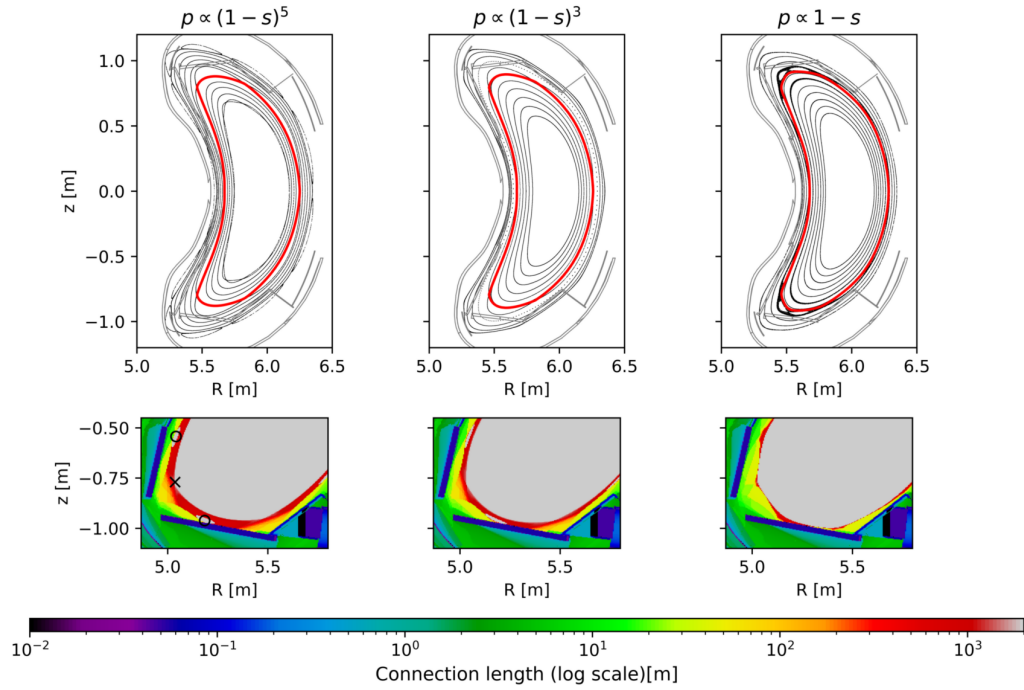
Figure 16: Plasma response in high-iota configuration at fixed axial beta ($\beta_{ax} = 5\%$) to changes in pressure profile shape, with $p \propto (1 - s)^5$ (left), $p \propto (1 - s)^3$ (center) and $p \propto 1 - s$ (right). Analog to figure 15.

Figure 17: Divertor heat load distributions in low-iota configuration for different central beta values

higher plasma beta at opposite island phase, due to the plasma-driven magnetic field component overcoming the vacuum magnetic field. The required central beta values (around 7%) are, however, probably outside of the near-term experimentally achievable range.

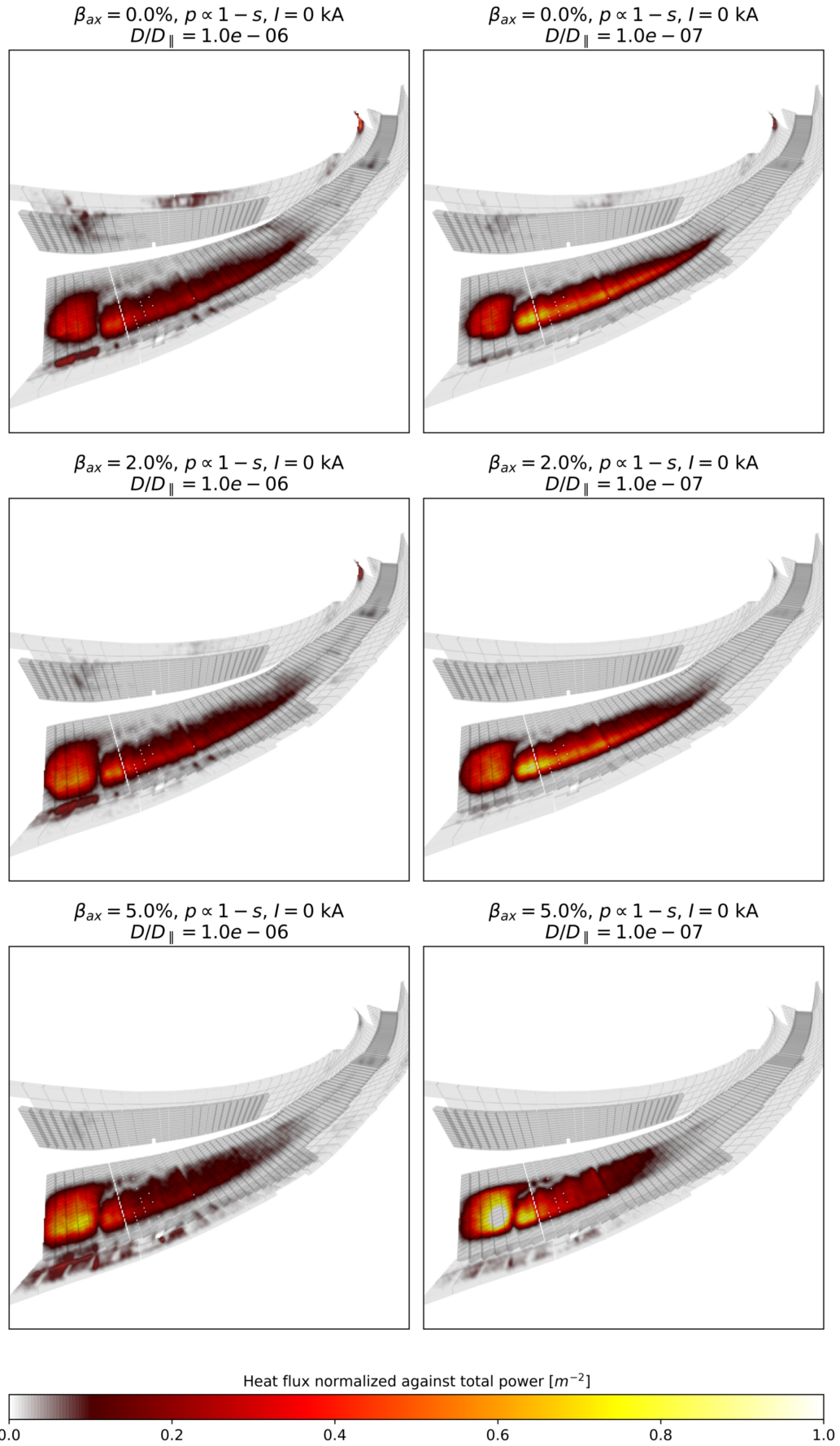## 4.4 General Statements

For the beta ranges foreseen in the upcoming water-cooled divertor campaign, the following general statements can be made:

- The high- and low-iota sections of the divertor plate appear to be safe for high-power operation in all scenarios except high-iota operation combined with low $D/D_\parallel$, where the narrow strike-line on the high-iota tail limits the power to about $6\,\mathrm{MW}$.

- The middle section, which has a restricted heat flux limitation of $0.5\,\mathrm{MW\,m^{-2}}$, generally imposes the strictest divertor load limit of all four target sections.

- In almost all scenarios, the power-limit related to hot-spots on the baffles is far below the limit of the divertor plates themselves. The relevance of this limit is difficult to assess, as the baffles do not form a smooth geometry, and most of the loads are on or near the edges of the baffle tiles. Even a small amount of erosion of the tiles at their edges during operation might potentially even out these loads sufficiently to prevent further harm to the baffles.

- In high-iota configuration, it is cruicial to avoid overloading the U-port areas, since more heat flows into this region during high-beta operation.

- Depending on the edge diffusion coefficient, large heat loads should be expected on the baffles during high-beta low-iota operation due to the limiter-like equilibrium topology. These loads are not toroidally elongated and focus a significant fraction of the heat onto a few tiles. These loads could potentially be controlled by shifting the radial magnetic axis location through a vertical field generated by asymmetric planar coil currents.

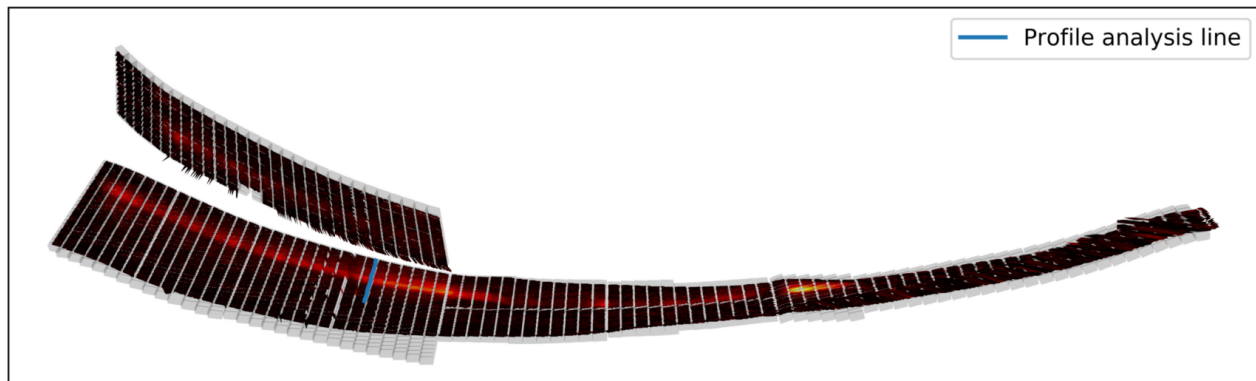# 5 Comparison between simulations and experimental measurements

Whilst modeling of the high-beta plasma scenarios is relevant for the upcoming campaigns, it is equally important to determine the limitations of the used model by comparing it to available experimental data. A cursory comparison (figure 18) of divertor heat-flux measurements by divertor infrared (IR) cameras [32] to cor-responding equilibria / field line diffusion modeling indicates apartial agreement between experimental observation and its synthesized equivalent on the main strike-line positions. The wider sections of the strike-line and the secondary loads on the middle and the high-iota section of the main divertor plate appear to be decently reproduced by the anisotropic diffusion model. However, the simulation does not reproduce the thinner components of the main strike-line.. Similarly, the vertical target heat loads do not fully agree on the heat load shape. However, the general deposition locations are still comparable. The experimental strike-line width exhibits a deviation between the upper and lower divertors, with the lower divertors (viewed from port AEF30 as an example in figure 18) showing generally wider strike-line patterns than the upper divertors (example being viewed from port AEF31 in figure 18). This could be attributed to particle drifts during their motion along the field lines (discussed in more detail in [31]), which are not modeled by our diffusion model. Finally, non-linear anomalous transport effects are not captured by our model, as it is inherently linear.

For a more quantitative comparison of the model and experimental measurements, we chose the distance of the strike-line from the pumping gap along the blue line shown in figure 18 as a target value.The change in strike-line position was then approximated by a linear regression in central beta, peaking factor and toroidal plasma current. For sufficient statistical volume, we sampled all discharges from August 14th 2018 at $1\,\mathrm{s}$ intervals (except those where the magnetic configuration was modified with control coils, and discharge no. 7 due to a failure in the data pipe-line). The plasma pressure profiles were approximated as outlined in section 3.1, and are exemplarily shown in figure 19. To prevent an excessive influence of outliers in the pressure profile on the fit, and to ensure that pressure-profiles strongly deviant from the $(1 - s)^\alpha$-shape do not cause additional hidden correlations, an upper threshold was placed on the χ^2 functional of the fit. For comparison, a synthetic dataset covering the same range of pressure profiles was built from HINT equilibria. In particular, the following parameters were determined for both experimental and synthetic data:

- On-axis plasma beta ("central beta"), defined as $\beta_{\mathrm{axis}} = 2\mu_0 p_{\mathrm{axis}}/B_0^2$ with B_0 being the average magnetic field along the axis, obtained experimentally by fitting plasma parameter profiles as in section 3.1

- Peaking factor $(\beta_{\mathrm{axis}}/\beta_{\mathrm{volavg}})$ of the pressure profile, approximated as $\frac{p(0)}{\int_0^1 p(r^2)r dr}$ with $p(s) = (1-s)^\alpha$, with r being the normalized minor radius and $s \approx r^2$ being the normalized toroidal flux

- Toroidal plasma current measured by Rogowski coils [33]

Experimental heat-flux
$\beta_{ax} = 1.8\%, I_{tor} = 85A, P_{ECRH} = 3.2MW, P_{rad} \approx 1.1MW$
#20180814.009, $t - t_0 = 2.0s$
Port AEF30 (Lower divertor)

— Profile analysis line

Port AEF31 (Upper divertor)

— Profile analysis line
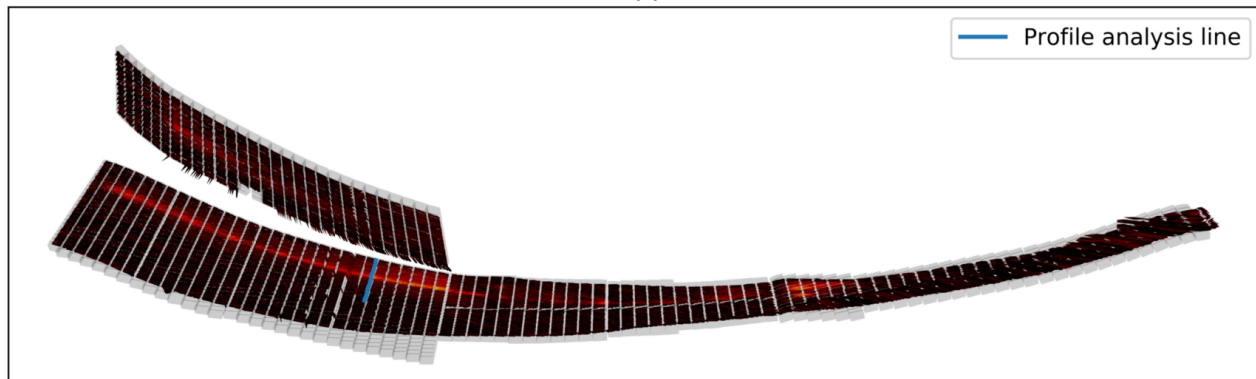
Field-line Diffusion $\beta_{ax} = 2.0\%, I_{tor} = 7A, p \propto (1-s)^{3.0}, D/D_{\parallel} = 10^{-6}$

— Profile analysis line
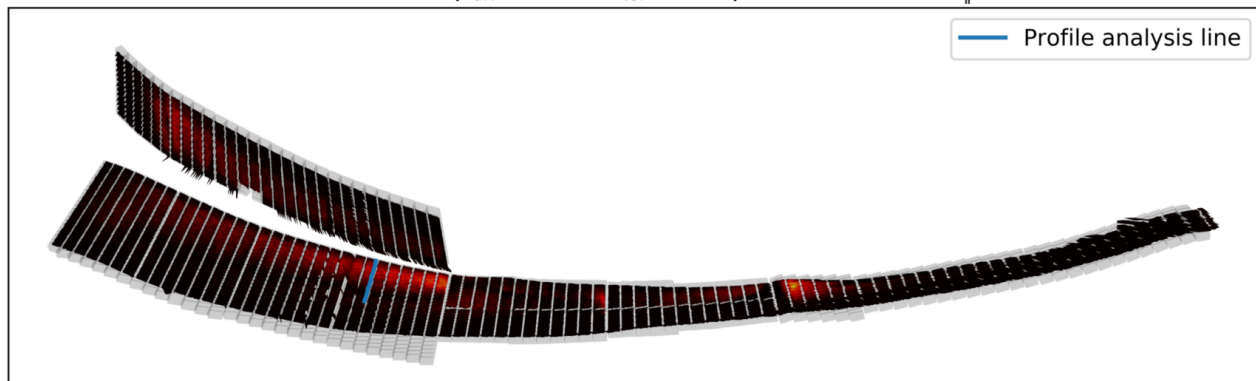
Heat-flux normalized against total power [m^{-2}]

Figure 18: Comparison of an infrared observation sample (upper divertor in module 3 as AEF31, lower divertor in module 3 as AEF30) and a corresponding heat-flux simulation
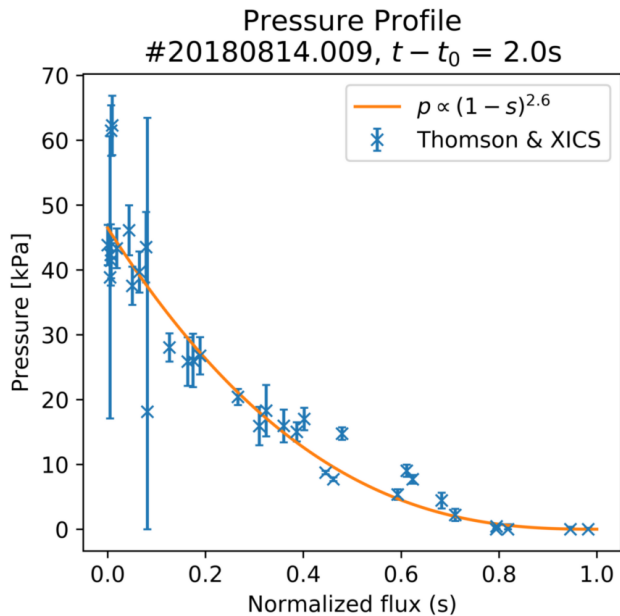
Figure 19: Pressure profile obtained from XICS and Thomson Scattering, as well as reduced degree-of-freedom fit to $p = p_0 \cdot (1 - s)^\alpha$

The main motivation for choosing the strike-line position here is its robustness concerning local deviations in transport coefficients. The edge plasma transport behavior (commonly described by the Braginskii equations) is dependent on the temperature profile in the plasma edge. These nonlinear effects required to obtain a fully self-consistent description of the edge plasma are not captured by our modelling process, and are beyond the scope of this manuscript. At the same time, the plasma performance experimentally achieved so far in equilibrium is too low to properly observe most of the predicted changed in heat load patterns, which only set on around 4% central beta. Furthermore, a direct comparison of calculated and measured peak loads requires a robust global power balance estimation to correctly determine the overall power flowing onto plasma-facing components. Therefore, as the focus of this work is the analysis of plasma beta effects on the magnetic topology and the resulting changes in divertor heat loads, we chose a heat load feature primarily related to the topology. The resulting datasets for this feature are comparatively shown in figure 20.

After determining the strike-line positions from IR camera observations [32] of the individual divertors, the positions were averaged over all upper and lower divertor observations in modules 1 thorugh to 4. Only time-slices, where the strike-line could be observed with sufficient contrast in all eight cameras were included in the analysis. The change in strike-line position was then approximated by a linear regression in central beta, peak-

ing factor and toroidal plasma current. Errors on the linear fit parameters were estimated by repeatedly performing the same fit on subsamples of the dataset to obtain distributions of the fit parameters. Figure 21 shows a comparison of the predictions for strike-line distances based on the linear estimation against the data points in the dataset. The dataset appears to scatter beyond the uncertainty of the regression. This does not mean that the error bar on the fitted parameters is underestimated, but rather indicates the presence of nonlinearities and/or statistical fluctuations in the input data. The full datasets and the regression results are shown in figure 22. Both simulations and experiment do not showcase any significant shift of the strike-line with central beta over the dataset range. Simulations and experiment also both predict a tiny shift in the strike-line position due to pressure profile shape changes at fixed central beta (experiment: 4(4) mm, modeling: 1.6(12) mm ranging from peaking factor 2 to 6). The main driver for strike-line position changes in both datasets is the toroidal plasma current, which can shift the strike-line by 2 cm (experiment observation) when evolving in a range up to 5 kA. [2]Finally, the model appears to underestimate the distance between strike-line center and pumping gap by 6 mm to 1 cm. This offset is also present in low-beta current-effect studies and extends all the way down to the vacuum field. It is therefore most likely an effect of the field line diffusion model, and requires significantly more detailed and resource-intensive numerical modeling to overcome.

As visible in figure 23, there are also asymmetries in the strike-line position between the different IR camera observations, which violate the assumed symmetries of the model. Potential sources of these asymmetries could be helical error fields [35, 36], particle drifts along the path from the last-closed-flux surfaces to the divertor [31] or mismatches in the divertor geometry. Figure 23 also indicates that attempting to fit the asymmetries with a combination of helical 1/1,2/2 and up-down asymmetries does not satisfactorily model the variation between the different observation points, which indicates additional sources of asymmetry which are not up-down or low-order helical. Unfortunately, fitting additional higher helical modes would make the fit prone to overfitting.

6 Discussion, conclusion & outlook

Finite-beta equilibria were calculated with the HINT code to determine the changes in W7-X's edge magnetic field structure in future high-performance operation. The equilibrium magnetic fields were then analyzed

---

[2]The effects of the plasma current are not a subject of this study, but must be included in the analysis due to their strong influence. Please see [34] for a more in-depth study of the plasma current effects.
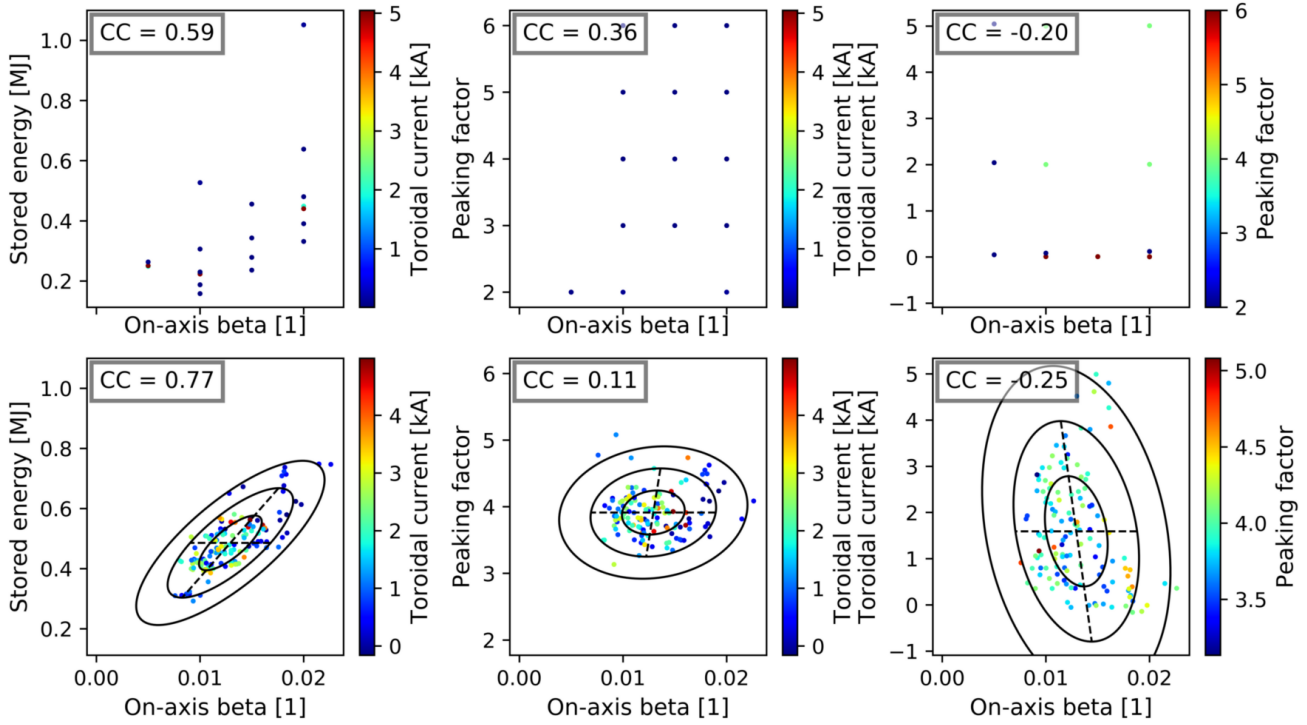
Figure 20: Overview of the grid of HINT runs (upper) and corresponding experimental data (lower). Ellipses mark the $1\sigma, 2\sigma$ and 3σ intervals around the data. Dashed lines indicate the principal components. Correlation coefficients between the displayed parameters are shown in the top-left corners.
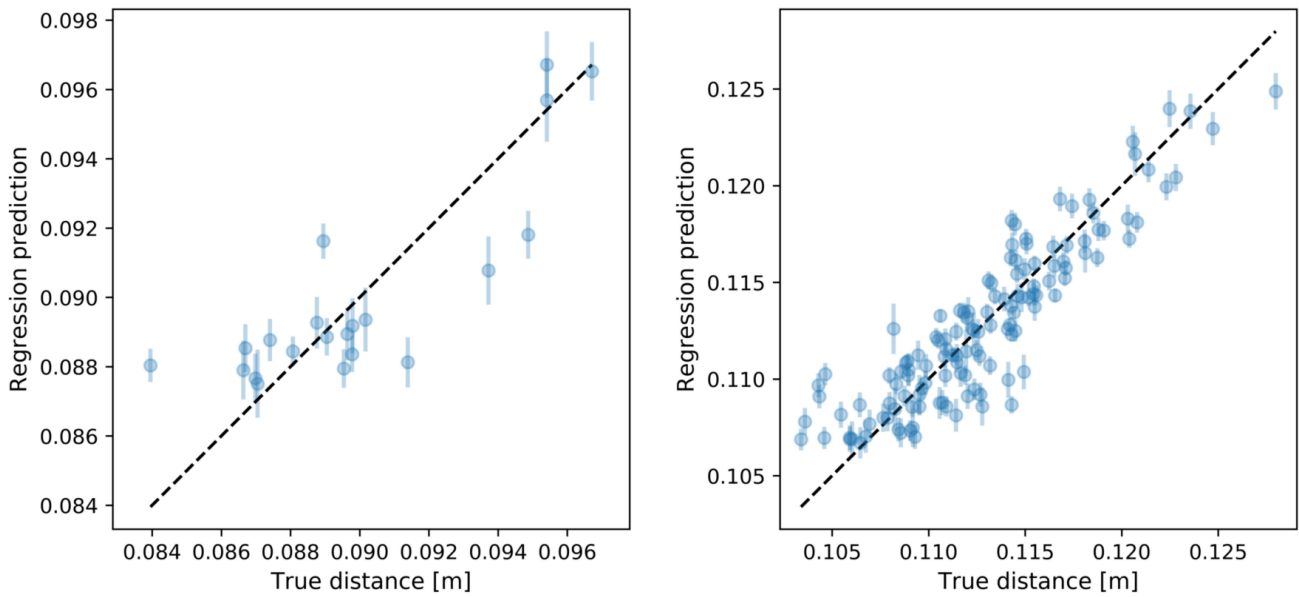
Figure 21: Prediction uncertainty (error bars) and errors (deviation from $y = x$-line) for the strike-line position regression in the synthetic (left) and the experimental dataset (right)
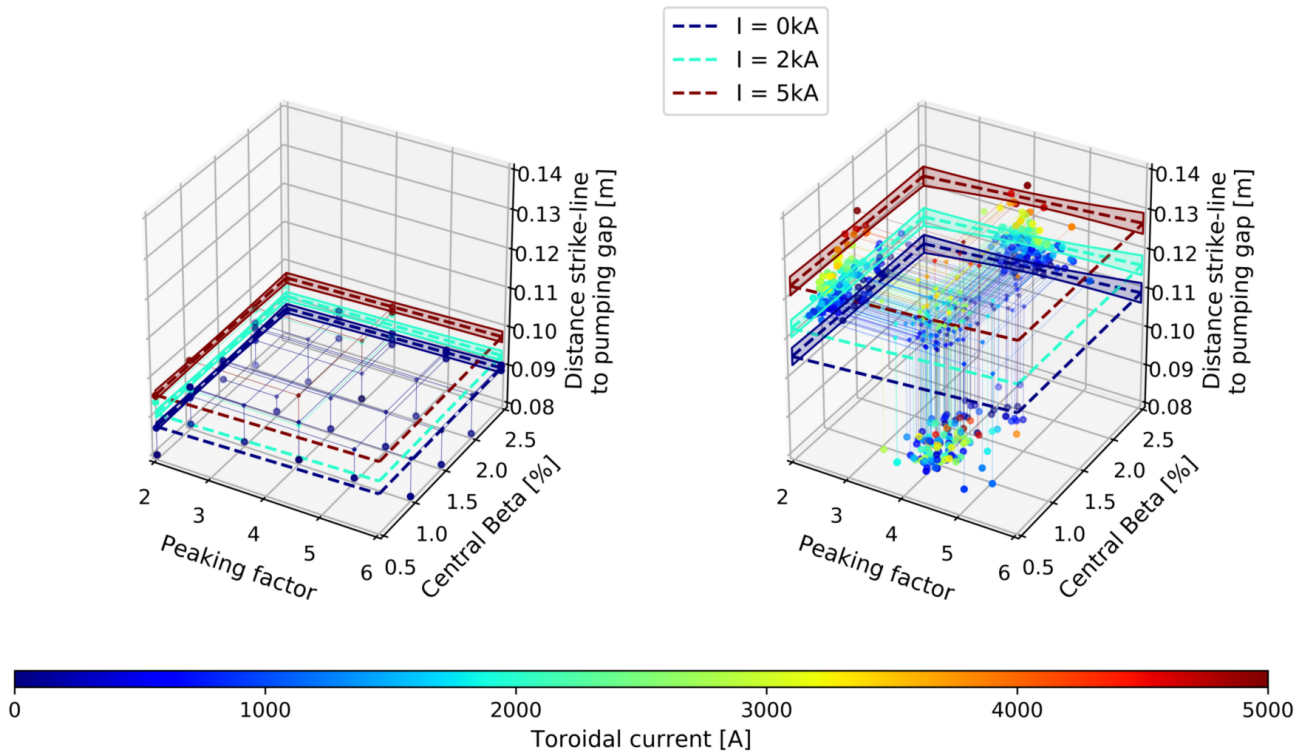
Figure 22: Full 4D datasets of central beta, pressure profile peaking factor, toroidal plasma current and distance from strike-line to pumping gap (small dots), connected to projections into 3D (with the third dimension indicated as color). Dashed planes represent the linear regression fit.
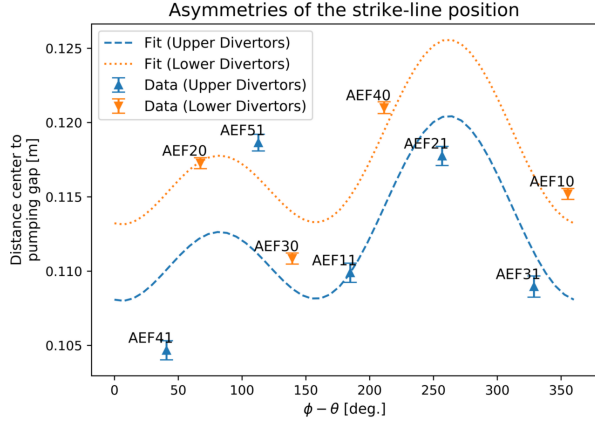
Figure 23: Per-divertor deviation of the strike-line position observations, together with an attempted fit combining an up-down-, a 1/1- and a 2/2-contribution. Values are plotted against the 1/1 helical angle. Dashed lines indicate the attempted fits for upper and lower divertors.

with field line diffusion methods to estimate the heat load distributions in future high-beta experimental programs. The standard ($\iota = 5/5$) configuration was found to be mostly stable against beta-driven topology changes with only moderate amounts of edge stochastization and the smallest change in divertor heat loads in finite-beta scenarios. The simulations were benchmarked in standard configuration by comparing predictions of the strike-line movement with a collection of discharges in identical vacuum configuration and with varying plasma parameters. The experimental benchmarks in moderate beta scenarios confirm the expected stability of the standard configuration against plasma-beta driven effects.

In the high-iota configuration we observe a lack of closed magnetic surfaces outside the edge islands in the calculations, which contributes to edge island stochastization at higher plasma beta. One might speculate, that this finding is caused by the iota-value being close to the upper end of the designed ι range of the coil system. The interaction of the edge islands with these outer stochastic regions leads to stochastization of the magnetic islands, accompanied by the appearance of loads on non-divertor PFCs in simulated high-beta scenarios, a situation which could be remedied by modification of the impacted heat-shield tiles. While the standard configuration also shows a certain degree of stochastization, it is substantially more stable than the high-iota configuration in this regard. Furthermore, the stochastization of the high-iota configuration appears to depend on the volume-averaged beta even at fixed on-axis beta, while the standard configuration is not exhibiting any such dependency.

The low-iota configuration exhibits the annihilation of the edge islands at high volume-averaged beta by the

$n/m = 5/6$ magnetic component driven by the finite-beta plasma with an opposite phase to the vacuum magnetic component. This leads to a transition towards a limiter-like magnetic configuration at a volume-averaged beta of 2.5%. In the limiter-like configuration, the divertor heat load distribution transitions from a limiter-like to a spot-like distribution. This makes the low-iota configuration unsuitable for long-pulse operation without further modification. However, this transition could provide a good quantitative benchmark of finite-beta heat load simulations if it can be safely experimentally realized.

Comparison with experimental measurements shows that not all heat load patterns in the experimental scenarios could be reproduced in the anisotropic diffusion modeling. Therefore, scenarios which appear operationally safe from these simulations should still be carefully experimentally explored. There are still a few degrees of freedom one could add to the modeling process to potentially better match the experimental observations. The diffusion coefficient ratio, which is currently a fixed input, could be varied based on spatial position (or lifetime) of the tracer particles. Additionally, drift terms could be added to attempt to model the asymmetries between upper and lower divertor targets. To achieve a broad physical agreement, however, will require more comprehensive simulation packages (such as EMC3). Therefore, finding methods to make these packages more amenable for magnetic configuration scans (e.g. by improving automatic grid generation) might yield more valuable long-term payoffs.

For more in-depth scenario modeling. there are still plenty of opportunities to improve the accuracy of the equilibrium calculations. While the chosen pressure distributions provide adequate fits to the core plasma profiles, their accuracy in the edge is yet to be determined. Additionally, the interaction of the beta effects with effects driven the toroidal plasma current needs to be addressed. Combining these effects into integrated scenario modeling is an important topic for further research. Another focal point is to address the same set of questions for the high-mirror magnetic configuration, which is optimimized for the lowest bootstrap current of all potential magnetic configurations.

Acknowledgements

References

[1] R. C. Wolf et al. "Performance of Wendelstein 7-X stellarator plasmas during the first divertor operation phase". In: *Physics of Plasmas* 26.8 (2019), p. 082504. DOI: 10.1063/1.5098761.

[2] Y. Liang et al. "Diagnostic set-up and modelling for investigation of synergy between 3D edge physics and plasma-wall interactions on Wendelstein 7-X". In: *Nuclear Fusion* 57.6 (May 2017), p. 066049. DOI: 10.1088/1741-4326/aa6cde.

[3] Oliver Schmitz et al. "Stable heat and particle flux detachment with efficient particle exhaust in the island divertor of Wendelstein 7-X". In: *Nuclear Fusion* (2020). URL: http://iopscience.iop.org/10.1088/1741-4326/abb51e.

[4] D. Zhang et al. "First Observation of a Stable Highly Dissipative Divertor Plasma Regime on the Wendelstein 7-X Stellarator". In: *Phys. Rev. Lett.* 123 (2 July 2019), p. 025002. DOI: 10.1103/PhysRevLett.123.025002.

[5] T. Sunn Pedersen et al. "First divertor physics studies in Wendelstein 7-X". In: *Nuclear Fusion* 59.9 (July 2019), p. 096014. DOI: 10.1088/1741-4326/ab280f.

[6] E Strumberger. "Finite- magnetic field line tracing for Helias configurations". In: *Nuclear Fusion* 37.1 (Jan. 1997), pp. 19–27. DOI: 10.1088/0029-5515/37/1/i03.

[7] E. Strumberger. "Stochastic Magnetic Field Structure in the Edge Region of W7-X". In: *Contributions to Plasma Physics* 38.1-2 (1998), pp. 106–111. DOI: 10.1002/ctpp.2150380115.

[8] Y. Suzuki et al. "Three-Dimensional Effects on Stochasticity in Non-Axisymmetric Tori". In: *Contributions to Plasma Physics* 50.6-7 (2010), pp. 576–581. DOI: 10.1002/ctpp.200900058.

[9] T. Hayashi et al. "Formation and 'self-healing' of magnetic islands in finite-β Helias equilibria". In: *Physics of Plasmas* 1.10 (1994), pp. 3262–3268. DOI: 10.1063/1.870478. eprint: https://doi.org/10.1063/1.870478.

[10] M Drevlak, D Monticello, and A Reiman. "PIES free boundary stellarator equilibria with improved initial conditions". In: *Nuclear Fusion* 45.7 (July 2005), pp. 731–740. DOI: 10.1088/0029-5515/45/7/022.

[11] Y Suzuki and J Geiger. "Impact of nonlinear 3D equilibrium response on edge topology and divertor heat load in Wendelstein 7-X". In: *Plasma Physics and Controlled Fusion* 58.6 (May 2016), p. 064004. DOI: 10.1088/0741-3335/58/6/064004.

[12] Yasuhiro Suzuki et al. "Development and application of HINT2 to helical system plasmas". In: *Nuclear Fusion* 46.11 (Sept. 2006), pp. L19–L24. DOI: 10.1088/0029-5515/46/11/l01.

[13] Yasuhiro Suzuki. "HINT modeling of three-dimensional tokamaks with resonant magnetic perturbation". In: *Plasma Physics and Controlled Fusion* 59.5 (Mar. 2017), p. 054008. DOI: 10.1088/1361-6587/aa5adc.

[14] Hauke Hölbe. "Control of the magnetic topology and plasma exhaust in the edge region of Wendelstein 7-X: A numerical study". PhD thesis. Ernst-Moritz-Arndt-Universität Greifswald, 2015.

[15] G. Bongiovì et al. "Assessment of potential heat flux overload of target and first wall components in Wendelstein 7-X finite-beta magnetic configurations and choice of locations for temperature monitoring". In: *Fusion Engineering and Design* 161 (2020), p. 111902. ISSN: 0920-3796. DOI: 10.1016/j.fusengdes.2020.111902.

[16] J Geiger et al. "Physics in the magnetic configuration space of W7-X". In: *Plasma Physics and Controlled Fusion* 57.1 (Nov. 2014), p. 014004. DOI: 10.1088/0741-3335/57/1/014004.

[17] H Renner et al. "Divertor concept for the W7-X stellarator and mode of operation". In: *Plasma Physics and Controlled Fusion* 44.6 (May 2002), pp. 1005–1019. DOI: 10.1088/0741-3335/44/6/325.

[18] Hermann Renner et al. "Physical Aspects and Design of the Wendelstein 7-X Divertor". In: *Fusion Science and Technology* 46.2 (2004), pp. 318–326. DOI: 10.13182/FST04-A570.

[19] M Drevlak, D Monticello, and A Reiman. "PIES free boundary stellarator equilibria with improved initial conditions". In: *Nuclear Fusion* 45.7 (July 2005), pp. 731–740. DOI: 10.1088/0029-5515/45/7/022.

[20] H. Peraza-Rodriguez et al. "Extension of the SIESTA MHD equilibrium code to free-plasma-boundary problems". In: *Physics of Plasmas* 24.8 (2017), p. 082516. DOI: 10.1063/1.4986447.

[21] T. Andreeva, J. Kisslinger, and H. Wobig. "Characteristics of main configurations of Wendelstein 7-X". In: *Problems of Atomic Science and Technology. Series: Plasma Physics* 35 (7 2002), pp. 45–47.

[22] E. Pasch et al. "The Thomson scattering system at Wendelstein 7-X". In: *Review of Scientific Instruments* 87.11 (2016), 11E729. DOI: `10.1063/1.4962248`.

[23] S.A. Bozhenkov et al. "The Thomson scattering diagnostic at Wendelstein 7-X and its performance in the first operation phase". In: *Journal of Instrumentation* 12.10 (Oct. 2017). DOI: `10.1088/1748-0221/12/10/p10004`.

[24] E.R. Scott et al. "Demonstration of an absolute Rayleigh scattering spectral calibration on the W7-X Thomson scattering system". In: *Journal of Instrumentation* 14.10 (Oct. 2019), pp. C10033–C10033. DOI: `10.1088/1748-0221/14/10/c10033`.

[25] N A Pablant et al. "Measurement of core plasma temperature and rotation on W7-X made available by the x-ray imaging crystal spectrometer (XICS)". In: *Invited papers to be published in a special issue of Plasma Physics and Controlled Fusion.* (July 2014).

[26] J. Kring et al. "In situ wavelength calibration system for the X-ray Imaging Crystal Spectrometer (XICS) on W7-X". In: *Review of Scientific Instruments* 89.10 (2018), 10F107. DOI: `10.1063/1.5038809`.

[27] M. Grahl et al. "Web Services for 3D MHD Equilibrium Data at Wendelstein 7-X". In: *IEEE Transactions on Plasma Science* 46.5 (2018), pp. 1114–1119. DOI: `10.1109/TPS.2017.2784903`.

[28] Jülich Supercomputing Centre. "JURECA: Modular supercomputer at Jülich Supercomputing Centre". In: *Journal of large-scale research facilities* 4.A132 (2018). DOI: `10.17815/jlsrf-4-121-1`.

[29] Y Feng et al. "Monte-Carlo fluid approaches to detached plasmas in non-axisymmetric divertor configurations". In: *Plasma Physics and Controlled Fusion* 59.3 (Feb. 2017), p. 034006. DOI: `10.1088/1361-6587/59/3/034006`.

[30] E Strumberger et al. *First Survey of Finite-beta Magnetic Fields of W7-X.* Tech. rep. Max-Planck-Institut für Plasmaphysik, Germany, 1997. URL: `http://hdl.handle.net/11858/00-001M-0000-0028-CFB7-1`.

[31] K C Hammond et al. "Drift effects on W7-X divertor heat and particle fluxes". In: *Plasma Physics and Controlled Fusion* 61.12 (Oct. 2019), p. 125001. DOI: `10.1088/1361-6587/ab4825`.

[32] Marcin Jakubowski et al. "Infrared imaging systems for wall protection in the W7-X stellarator (invited)". In: *Review of Scientific Instruments* 89.10 (2018), 10E116. DOI: `10.1063/1.5038634`.

[33] M. Endler et al. "Engineering design for the magnetic diagnostics of Wendelstein 7-X". In: *Fusion Engineering and Design* 100 (2015), pp. 468–494. ISSN: 0920-3796. DOI: `10.1016/j.fusengdes.2015.07.020`.

[34] Yu Gao et al. "Effects of toroidal plasma current on divertor power depositions on Wendelstein 7-X". In: *Nuclear Fusion* 59.10 (Aug. 2019), p. 106015. DOI: `10.1088/1741-4326/ab32c2`.

[35] Samuel A. Lazerson et al. "Error field measurement, correction and heat flux balancing on Wendelstein 7-X". In: *Nuclear Fusion* 57.4 (Mar. 2017), p. 046026. DOI: `10.1088/1741-4326/aa60e7`.

[36] Samuel A Lazerson et al. "Error fields in the Wendelstein 7-X stellarator". In: *Plasma Physics and Controlled Fusion* 60.12 (Nov. 2018), p. 124002. DOI: `10.1088/1361-6587/aae96b`.

A Reference table for divertor heat load distribution

Table 1 header spans multiple groups. Columns (left to right): Config., β_{ax}, $p(s)$, I_{tor} [kA], $D/D_\parallel$, $\int p\,dV$, Limit Divertor P_{max}, By, Baf. P_{max}, U-P. P_{max}, Peak Flux Divertor (V, HL, HM, HH, Total), Baf., U-P., Load Divertor (V, HL, HM, HH, Total), Baf., U-P., Wetted Area Divertor.

Config.	β_{ax}	$p(s)$	I_{tor} [kA]	$D/D_\parallel$	$\int p\,dV$	Limit Div. P_{max}	By	Baf. P_{max}	U-P. P_{max}	PF V	PF HL	PF HM	PF HH	PF Total	Baf.	U-P.	Load V	Load HL	Load HM	Load HH	Load Total	Baf.	U-P.	Wetted Area Div.
5/4	0.0	Vac	Vac	10^{-6}	0	0.7	HM	0.8	0.7	0.9	0.1	0.7	1.3	1.3	0.3	0.3	29%	8%	5%	56%	97%	2%	1%	0.8
				10^{-7}	0	0.8	HM	2.2	-	0.9	0.1	0.7	2.1	2.1	0.1	0.1	19%	3%	3%	75%	99%	0%	0%	0.5
	2.0	$(1-s)^{5.0}$	0.0	10^{-6}	221	0.9	HM	0.7	0.3	0.7	0.2	0.5	1.0	1.0	0.4	0.7	22%	10%	4%	52%	88%	4%	8%	0.8
				10^{-7}	221	0.8	HM	3.1	-	0.7	0.1	0.6	2.1	2.1	0.1	0.1	15%	3%	2%	80%	99%	0%	0%	0.5
		$1-s$	0.0	10^{-6}	868	0.8	HM	2.0	0.4	0.5	0.1	0.6	1.3	1.3	0.1	0.5	16%	7%	4%	70%	96%	1%	3%	0.7
				10^{-7}	868	0.9	HM	6.7	1.5	0.3	0.0	0.6	1.9	1.9	0.0	0.1	6%	2%	2%	89%	99%	0%	1%	0.5
	5.0	$(1-s)^{3.0}$	0.0	10^{-6}	768	0.8	HM	3.5	0.5	0.4	0.1	0.6	1.2	1.2	0.1	0.4	12%	7%	4%	73%	96%	1%	3%	0.8
				10^{-7}	768	0.9	HM	0.4	0.0	0.4	1.0	0.5	1.7	1.7	0.6	4.2	6%	4%	1%	73%	84%	3%	13%	0.5
		$(1-s)^{5.0}$	0.0	10^{-6}	541	0.9	HM	1.0	0.6	0.4	0.1	0.6	1.2	1.2	0.2	0.3	14%	8%	4%	70%	96%	1%	3%	0.8
				10^{-7}	541	1.0	HM	5.5	1.1	0.3	0.0	0.5	1.8	1.8	0.0	0.2	9%	3%	2%	85%	98%	0%	1%	0.6
		$1-s$	0.0	10^{-6}	1609	1.0	HM	2.4	0.3	0.1	0.1	0.5	1.1	1.1	0.1	0.8	4%	6%	3%	78%	92%	1%	7%	0.8
				10^{-7}	1609	1.1	HM	8.1	0.1	0.1	0.0	0.5	1.6	1.6	0.0	1.9	1%	2%	1%	91%	95%	0%	4%	0.5
5/5	0.0	Vac	Vac	10^{-6}	0	1.4	HM	1.0	-	0.4	0.5	0.4	0.7	0.7	0.3	0.0	27%	42%	14%	9%	92%	8%	1%	1.3
				10^{-7}	0	1.3	HM	2.1	-	0.6	0.7	0.4	0.4	0.7	0.1	0.0	23%	62%	9%	4%	97%	3%	0%	1.3
	2.0	$(1-s)^{3.0}$	0.0	10^{-6}	480	1.6	HM	1.5	-	0.3	0.5	0.3	0.5	0.5	0.2	0.0	26%	46%	12%	8%	92%	8%	1%	1.7
				10^{-7}	480	1.8	HM	4.4	-	0.5	0.7	0.3	0.3	0.7	0.1	0.0	25%	64%	6%	3%	98%	2%	0%	1.4
		$(1-s)^{5.0}$	0.0	10^{-6}	331	1.4	HM	1.4	-	0.3	0.5	0.4	0.6	0.6	0.2	0.0	26%	45%	13%	8%	92%	8%	1%	1.6
				10^{-7}	331	1.9	HM	3.8	-	0.5	0.7	0.3	0.3	0.7	0.1	0.0	24%	65%	6%	3%	98%	2%	0%	1.3
		$1-s$	0.0	10^{-6}	1052	1.8	HM	1.8	-	0.3	0.4	0.3	0.5	0.5	0.1	0.1	24%	47%	12%	9%	92%	8%	1%	1.7
				10^{-7}	1052	2.1	HM	4.8	-	0.5	0.7	0.2	0.3	0.7	0.1	0.0	23%	65%	6%	3%	98%	2%	0%	1.4
	5.0	$(1-s)^{3.0}$	0.0	10^{-6}	1091	1.8	HM	2.3	-	0.3	0.4	0.3	0.5	0.5	0.1	0.1	26%	49%	10%	7%	92%	8%	1%	2.0
				10^{-7}	1091	2.1	HM	3.1	-	0.5	0.7	0.2	0.3	0.7	0.1	0.0	33%	59%	4%	2%	98%	2%	0%	1.4
		$(1-s)^{5.0}$	0.0	10^{-6}	792	1.7	HM	2.0	-	0.3	0.4	0.3	0.5	0.5	0.1	0.0	26%	48%	11%	7%	92%	8%	1%	1.8
				10^{-7}	792	2.0	HM	5.3	-	0.5	0.7	0.3	0.3	0.7	0.0	0.0	30%	62%	4%	2%	98%	2%	0%	1.4
		$1-s$	0.0	10^{-6}	2584	2.5	HM	0.7	0.7	0.3	0.4	0.2	0.3	0.4	0.3	0.3	19%	52%	8%	8%	86%	12%	2%	2.1
				10^{-7}	2584	2.4	HM	1.2	-	0.5	0.7	0.2	0.2	0.7	0.2	0.1	27%	64%	3%	2%	95%	4%	0%	1.4
			5.0	10^{-6}	2422	2.8	HM	0.9	0.7	0.3	0.3	0.2	0.3	0.3	0.3	0.3	21%	52%	8%	8%	88%	10%	1%	2.7
				10^{-7}	2422	3.0	HM	1.9	-	0.6	0.6	0.2	0.2	0.6	0.1	0.1	28%	64%	3%	2%	97%	3%	0%	1.6
			10.0	10^{-6}	2442	2.5	HM	0.9	0.8	0.3	0.3	0.2	0.3	0.3	0.3	0.2	21%	52%	7%	9%	89%	10%	1%	2.8
				10^{-7}	2442	3.3	HM	2.2	-	0.6	0.5	0.2	0.2	0.6	0.1	0.1	26%	66%	3%	2%	97%	2%	0%	1.7
5/5 HM	0.0	Vac	Vac	10^{-6}	0	2.7	HM	0.3	-	0.9	0.4	0.2	0.6	0.9	0.8	0.0	61%	16%	6%	4%	84%	15%	1%	0.9
				10^{-7}	0	2.5	HM	0.5	-	1.1	0.4	0.2	0.3	1.1	0.6	0.0	79%	12%	2%	2%	93%	7%	0%	0.9
	2.0	$1-s$	0.0	10^{-6}	856	3.1	HM	0.4	-	0.7	0.3	0.2	0.5	0.7	0.6	0.1	63%	16%	5%	5%	87%	12%	1%	1.3
				10^{-7}	856	3.2	HM	0.8	-	1.1	0.4	0.2	0.4	1.1	0.3	0.0	82%	10%	2%	2%	95%	5%	0%	0.9
	5.0	$(1-s)^{3.0}$	0.0	10^{-6}	903	3.2	HM	0.7	-	0.5	0.3	0.2	0.5	0.5	0.4	0.1	61%	18%	5%	4%	87%	12%	1%	1.6
				10^{-7}	903	2.9	HM	0.8	-	0.9	0.5	0.2	0.3	0.9	0.3	0.0	78%	13%	2%	2%	94%	5%	0%	1.1
		$(1-s)^{5.0}$	0.0	10^{-6}	626	2.8	HM	0.5	-	0.6	0.3	0.2	0.5	0.6	0.5	0.1	62%	18%	5%	4%	86%	12%	1%	1.5
				10^{-7}	626	2.8	HM	1.6	-	1.0	0.5	0.2	0.3	1.0	0.2	0.0	79%	13%	2%	2%	95%	5%	0%	1.0
		$1-s$	0.0	10^{-6}	2113	3.4	HM	0.7	0.9	0.6	0.3	0.1	0.4	0.6	0.4	0.2	57%	22%	4%	5%	87%	10%	2%	1.5
				10^{-7}	2113	3.0	HM	0.7	-	0.9	0.5	0.2	0.2	0.9	0.4	0.1	74%	18%	1%	1%	94%	5%	0%	1.0
5/6	0.0	Vac	Vac	10^{-6}	0	5.1	HM	0.2	-	0.1	0.5	0.1	0.1	0.5	1.3	0.0	3%	72%	5%	1%	80%	18%	2%	1.6
				10^{-7}	0	4.4	HM	0.4	-	0.0	0.9	0.1	0.0	0.9	0.7	0.0	1%	92%	2%	0%	95%	5%	0%	1.1
	2.0	$(1-s)^{5.0}$	0.0	10^{-6}	363	5.4	HM	0.3	-	0.1	0.5	0.1	0.1	0.5	0.9	0.0	2%	76%	5%	1%	83%	15%	2%	1.5
				10^{-7}	363	5.6	HM	0.7	-	0.0	0.9	0.1	0.0	0.9	0.4	0.0	1%	94%	2%	0%	96%	3%	0%	1.1
		$1-s$	0.0	10^{-6}	1145	6.0	HM	0.4	-	0.1	0.6	0.1	0.1	0.6	0.6	0.0	1%	82%	4%	1%	88%	11%	1%	1.4
				10^{-7}	1145	8.2	HM	2.0	-	0.0	1.0	0.1	0.0	1.0	0.1	0.0	0%	96%	2%	0%	98%	2%	0%	1.0
	5.0	$(1-s)^{3.0}$	0.0	10^{-6}	1007	6.8	HM	0.6	-	0.1	0.7	0.1	0.0	0.7	0.4	0.0	1%	84%	4%	1%	88%	11%	1%	1.3
				10^{-7}	1007	8.3	HM	3.9	-	0.0	0.9	0.1	0.0	0.9	0.1	0.0	0%	96%	1%	0%	98%	2%	0%	1.1
		$(1-s)^{5.0}$	0.0	10^{-6}	691	6.1	HM	0.4	-	0.1	0.6	0.1	0.0	0.6	0.6	0.0	1%	81%	4%	1%	86%	12%	1%	1.4
				10^{-7}	691	8.1	HM	1.7	-	0.0	0.9	0.1	0.0	0.9	0.1	0.0	0%	95%	2%	0%	97%	2%	0%	1.1
		$1-s$	0.0	10^{-6}	2203	6.3	HM	1.3	-	0.0	0.8	0.1	0.0	0.8	0.2	0.0	0%	83%	3%	0%	87%	12%	1%	1.1
				10^{-7}	2203	8.2	HL	2.5	-	0.0	1.2	0.0	0.0	1.2	0.1	0.0	0%	96%	1%	0%	96%	3%	0%	0.8

Table 1: Overview table of calculated power-normalized heat loads depending on magnetic configuration and pressure profile. Shown are integrated load distributions, peak normalized heat-fluxes and peak-flux related heating power limits (shown separately for divertor target with indication of the limiting section, baffle tiles and U-port). Divertor sections and baffles are labeled according to figure 3. U-port is abbreviated as "U.-P.". Limits are expressed in MW, normalized peak fluxes in m^{-2}, wetted area in m^2 and stored energy in kJ.